École polytechnique de Louvain

Spin wave emission by spin transfer torque

for beyond CMOS logic application

Author: **Raphaël Dawant**
Supervisors: **Florin Ciubotaru, Luc Piraux**
Readers: **Jean-Pierre Raskin, Flavio Abreu Araujo, Firstname Lastname**
Academic year 2018–2019
Master [120] in Physical Engineering

"Innovation, as I understand it, is both about doing different things as well as doing things differently."

Kiran Mazumdar-Shaw

UNIVERSITÉ CATHOLIQUE DE LOUVAIN

Abstract

Louvain School of Engineering

Master [120] in Physical Engineering

Spin wave emission by spin transfer torque

by Raphaël DAWANT

Spin wave devices are a promising alternative to realize logic circuits based on wave computing. The field is referred also as Magnonics. Spin waves (and their quanta: magnons) are used to transmit, and process signals in magnetic waveguides and the logic functions are performed by wave interference. The low power consumption and the possibility to scale down the are of the logic function have drawn significant interest in this field. To be integrated with CMOS technology, spin wave devices require efficient transducers to emit and detect magnons with an electrical current or voltage. It has been shown that transducers based on spin-transfer torque (STT) emission could be potential candidates. This experimental thesis consisted in the study of material and devices towards efficient spin wave emission by STT. Specific orthogonal magnetic tunnel junction stacks have been prepared, and their static and dynamic properties have been characterized at blanket and device level. Process development has been additionally completed to fabricate devices for spin wave excitation via STT.

This thesis was performed at IMEC facilities in Leuven, an international research center active in the fields of nanoelectronics.

Acknowledgements

I would like to start by thanking my supervisors; Florin Ciubotaru, for giving me the opportunity to realize my master's thesis in an international research center like IMEC and for introducing me in the words of spin waves, and Luc Piraux for having supported this project.

I would like to thank Diogo Costa in IMEC and Flavio Abreu Araujo from UCL for giving me insights about STT and STNO. Thank you Frederic Vanderveken for always answering my questions with enthusiasm, thanks to you I succeeded to see clear through this demagnetization field.

I would like to thanks my little sister to have endured me during the writing of this thesis and my godmother for all the support she gave me all over my studies.

I would like to give a special thanks to Giacomo Talmelli for the great support he gave me all this year, and for being always available to help me, most of the knowledge I learned this year comes from him. Thank you for your time and for the long proofreading of this manuscript.

Contents

List of Figures

List of Tables

List of Abbreviations

IMEC	Interuniversitair Micro-Elektronica Centrum
LLG	Landau-Lifshitz- Gilbert equation
STT	Spin Transfer Torque
SW	Spin Wave
FMR	Ferromagnetic Resonance
MSW	Magnetostatic Waves
MSSW	Magnetostatic Surface Wave
FVMSW	Forward Volume Magnetostatic Wave
BVMSW	Backward Volume Magnetostatic Wave
CMOS	Complementary Metal Oxide Semiconductor
SWMG	Spin Wave Majority Gate
STNO	Spin Torque Nano-Oscillators
MTJ	Magnetic Tunnel Junction
TMR	Tunnel Magnetoresistance
SAF	Synthetic Antiferromagnet
FL	Free Layer
PLs	Perpendicular Layers
PMA	Perpendicular Magnetic Anisotropy
VSM	Vibrating-Sample Magnetometer
SEM	Scanning Electron Microscopy
ER	Etching Rate
ET	Etching Time
VNA	Vector Network Analyzer

Introduction

Moore's law end is coming. As the transistor scaling reaching the wall of physics, the threatens of a lack of alternative have drawn the semiconductor industry in 'the king is dying' period[1]. During the last decades, the industry has placed numerous resources for *more Moore* miniaturization but has only face up to the hopelessness to cross the Wall. In these uncertain times, a new strategy has emerged: *more than Moore*. The only hope to maintain the increases of the performance is to progress through the diversification and the complexification of electronic systems.

In the last years, spintronic has drawn increased interest to build new logic systems. One branch of this field is called magnonics, from the spin wave quanta: magnons. Spin wave logic is based on wave computation; the Boolean value is carried by the phase, and the logic functions are performed by interference. This field can decrease the function footprint of a logic device with low power consumption.

Spin wave devices require an efficient mechanism for magnons emission and detection, compatible with CMOS technology. The goal of this thesis is to study and develop a new type of transducer based on spin-transfer torque for spin wave emission. The work include the development and the fabrication of spin wave devices as well as the electrical characterization of these devices.

The first chapter will be dedicated to the theoretical background of magnetism and spin waves. Starting from the magnetic dynamics and the spin-transfer torque effect, the concept of spin waves propagation in ferromagnetic materials will be presented.

The second chapter will detail the context of this project and the motivation of the technology. The general working principle of spin wave devices will be delivered, followed by the presentation of the devices of interest based on magnetic tunnel junction stack.

The third chapter will be present in detail the development and the fabrication process of two devices; one for the study of the spin wave propagation inside the materials used, and the other for the characterization of the spin waves emission by spin-transfer torque.

Finally, the last chapter will be devoted to the electrical characterization of the first devices. This section will aim to understand the effect of the complex magnetic stack on the spin waves propagation.

[1] This locution, coming from here[1], is for me a good illustration of how scientists can sometimes give a dramatic tone to the end of this conjecture, called law; forgetting that, at least in the beginning, it was mostly the forecast of a business plan.

Chapter 1

Theoretical background

In a material, the angular momentum $\boldsymbol{J}$ ($Kg\ m^2\ s^{-1}$) of the electrons in the atom creates a magnetic moment $\boldsymbol{\mu}$ ($A\ m^2$). The total angular momentum has two different contributions, one is the orbital angular momentum and the other is the intrinsic spin angular momentum. This magnetic moment and the angular momentum are linked by the gyromagnetic ratio γ ($s^{-1}\ T^{-1}$):

$$\boldsymbol{\mu} = \gamma \boldsymbol{J}. \tag{1.1}$$

In a magnetic material, the net magnetic moment is non-zero. The total magnetic moment of a magnetic sample is the sum of all the magnetic moment carried by each atom and the behavior of a magnetic system is described by the magnetization $\boldsymbol{M}$. It is defined as the number of magnetic moment per unit of volume:

$$\boldsymbol{M} = \frac{\sum_i \boldsymbol{\mu_i}}{V}, \tag{1.2}$$

and has the same unit as the magnetic field (A/m).

When a ferromagnetic material is subject to a magnetic field $\boldsymbol{H}$, the magnetization is given by the relationship:

$$\boldsymbol{M} = \boldsymbol{M_{sp}} + \chi_m \boldsymbol{H}, \tag{1.3}$$

where $\boldsymbol{M_{sp}}$ is the spontaneous magnetization and χ_m the magnetic susceptibility. Generally, the response of the magnetization $\boldsymbol{M}$ is anisotropic and non-linear, this means the susceptibility tensor χ_m is asymmetric and varies with $\boldsymbol{H}$. When $\boldsymbol{H}$ is large, all the magnetic moment aligned themselves in the direction of the field $\boldsymbol{H}$ and the magnetization $\boldsymbol{M}$ saturate to a constant value M_s as shown on Fig.1.1.

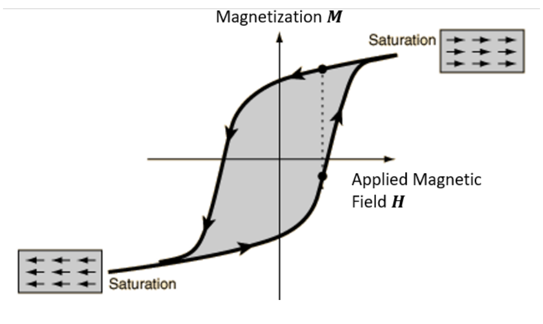

FIGURE 1.1: Hysteresis loop a ferromagnetic material. When the material is under a magnetic field, the magnetic moments aligned themselves in the direction of the field, increasing the net magnetic moment (magnetization). When all the magnetic moments are aligned, the magnetization saturated to a M_s value.[2]

The magnetic response depends also on the history of the system and is thus usually not reversible. This phenomenon creates a hysteresis loop in the response of the magnetization $\boldsymbol{M}$ (see Fig.1.1). The width of the loop is characterized by the coercive field $\boldsymbol{H_c}$, defined as the field $\boldsymbol{H}$ for a magnetization $\boldsymbol{M} = 0$, coming from a state where the state is fully saturated.

The area of the loop is related to the amount of energy dissipated during a change of magnetization and depend on the material. For a high coercive field $\boldsymbol{H_c}$, the magnetic field $\boldsymbol{H}$ required to change the magnetization is high, this system is, therefore, useful for permanent magnets and memory devices where high stability of the magnetization is required. For a low $\boldsymbol{H_c}$, only a small amount of energy is required to change the magnetization.

1.1 Effective field

In a magnetic material, the field inside the medium is not only due to the external field but also from different contribution created by the medium itself. The effective field $\boldsymbol{H_{eff}}$ referred to the field "felt" locally by the magnetization. It is defined as the derivative of the magnetic energy respected to the magnetization:

$$\boldsymbol{H_{eff}} = \frac{1}{\mu_0} \frac{d^2 E}{d\boldsymbol{M} dV}, \tag{1.4}$$

where μ_0 is the vacuum permeability and E the sum of all the magnetic energy coming from all the magnetic interaction. $\boldsymbol{H_{eff}}$ can be described as a sum of fields that derived from all the magnetic energy contribution:

$$\boldsymbol{H_{eff}} = \boldsymbol{H_{ext}} + \boldsymbol{H_{exch}} + \boldsymbol{H_{dip}} + \cdots, \tag{1.5}$$

where the term on the left side represent respectively: the external field, the exchange field and, the dipolar field. Other contributions exist, coming from for example to the magnetocrystalline anisotropy or the magnetostrictive effect but we will not focus on this other terms in this section.

External Field $\boldsymbol{H_{ext}}$

H_0 is the external field that derived from the Zeeman energy describes the interaction between the magnetization and external field:

$$E_Z = -\mu_0 \int_V \boldsymbol{M} \cdot \boldsymbol{H_{ext}} dV, \tag{1.6}$$

where μ_0 is the permeability of free space.

Exchange Field $\boldsymbol{H_{exch}}$

The exchange Field originates from the exchange interaction. This interaction originates from a quantum effect, due to an overlap of the wave function of the electron and Fermi exclusion principle, the magnetic moments of the electrons are coupled with each other. In the Heisenberg model, for a system with N spins, the exchange energy is described by [3]:

$$E_{exch} = -2\sum_{i}^{N}\sum_{j}^{N} J_{i,j}^{ex}\boldsymbol{S_i}\cdot\boldsymbol{S_j}, \tag{1.7}$$

where $J_{i,j}^{ex}$ is the exchange integral that describes the interaction between two spins. E_{exch} can also be described as a phenomenological continuum description:

$$E_{exch} = A\int_V \left((\nabla M_x)^2 + (\nabla M_y)^2 + (\nabla M_z)^2\right) dV, \tag{1.8}$$

where A is the exchange stiffness constant, A is linked to the exchange integral $J_{i,j}^{ex}$ and depend on the lattice structure. By inserting this equation in (1.4), the expression of the exchange field is given by:

$$\boldsymbol{H_{exch}} = -\lambda_{ex}^2\Delta\boldsymbol{M} \qquad \text{with} \qquad \lambda_{ex} = \frac{2A}{\mu_0 M_s^2}. \tag{1.9}$$

λ_{ex} is the exchange constant and is linked to the exchange length: $l_{ex} = \lambda_{ex}^2$. l_{ex} is the characteristic length range of the exchange interaction and it is in the order of few nanometers.

Dipolar Field H_{dip}

Each magnetic moments creates a magnetic field in the sample by dipolar interaction. The dipolar Field H_{dip} is the sum of all the fields created by each magnetic moments and is, therefore, the field created by the magnetization upon itself. The expression of the dipolar field can be directly deduced from the Maxwell equation when the electric current is zero:

$$\begin{cases} \nabla\cdot\boldsymbol{B} = 0. & (1.10)\\ \nabla\times\boldsymbol{H} = 0. & (1.11)\end{cases}$$

Since $\boldsymbol{B} = \mu_0(\boldsymbol{H}+\boldsymbol{M})$, these equations can be expressed as:

$$\begin{cases} \nabla\cdot\boldsymbol{H} = -\nabla\cdot\boldsymbol{M}. & (1.12)\\ \nabla\times\boldsymbol{H} = 0. & (1.13)\end{cases}$$

The solution of thess equations gives the expression of the dipolar field:

$$\boldsymbol{H_{dip}} = -\frac{1}{4\pi}\int_V \nabla\cdot\boldsymbol{M}\frac{\boldsymbol{r}}{r^3}dV. \tag{1.14}$$

Inside the material, the direction of the dipolar field is on the other direction of the magnetization and act therefore against the magnetization, for this reason, the dipolar field inside the material is called the demagnetization field $\boldsymbol{H_{demag}}$ (the dipolar field outside of the material is called the *stray field*).

The demagnetization field $\boldsymbol{H_{demag}}$ strongly depends on the shape of the sample. A more common way to link $\boldsymbol{H_{demag}}$ to the magnetization is with a tensor $\hat{N}$ called the demagnetization tensor:

$$\boldsymbol{H_{demag}}(\boldsymbol{r}) = -\frac{1}{V}\int_V \hat{N}(\boldsymbol{r})\boldsymbol{M}(\boldsymbol{r})dV, \tag{1.15}$$

and if the magnetization is uniform, the expression is reduced as:

$$H_{demag}(r) = -\hat{N}(r)M. \quad (1.16)$$

$\hat{N}$ is defined by the shape of the sample and varies in every point of the medium. This means that generally, the demagnetization field is non-uniform even if the magnetization is uniform. The only exception is for an ellipsoidal shape with a uniform magnetization. In this case, $\hat{N}$ is constant over the volume and H_{demag} is uniform :

$$H_{demag} = -\hat{N}M. \quad (1.17)$$

For example, in a thin film with a normal $\hat{z}$, $N_{zz} = 1$ and all the other component of the tensor equal zero. This means that $H_{demag} = -M_z\hat{z}$, therefore the demagnetization tend to suppress the magnetization out of the plane film. For this reason, in a plane film, the magnetization tends to be aligned in the plane.

1.2 Magnetization dynamics

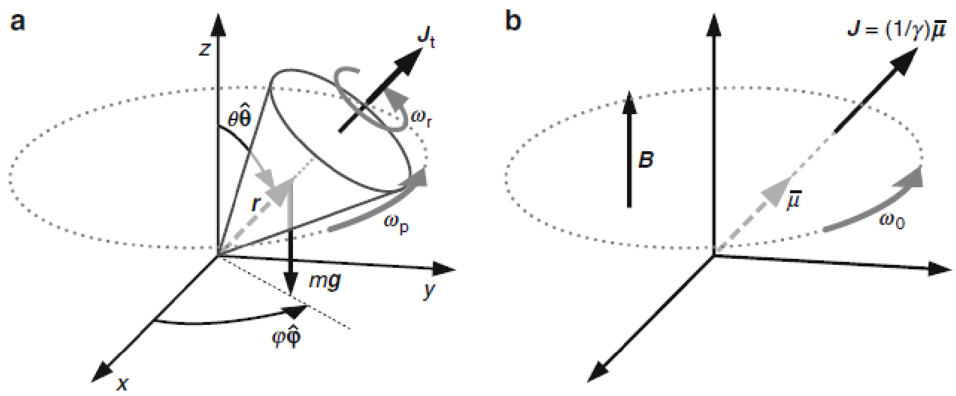

FIGURE 1.2: Illustration of the precessional movement. (a) Precession of a spin toy around the gravity axis; due to the angular momentum carried by the spin toy a torque, perpendicular to the gravity axis and the position vector ($r \times mg$), creates a precession movement. (B) In the same way, the angular momentum carried by the magnetic moments generates a precession movement around the magnetic field axis. [4]

At the equilibrium, the magnetization M is aligned in the direction of the effective field H_{eff} but, if due to a perturbation, the magnetization M deviates from the direction of the magnetic field, M will precess around H_{eff}. This is due to the angular momentum J creating a magnetic moment μ. Exactly like a spin toy (described by a vector position r) where the rate of change of the angular momentum is equal to the torque due to the gravity force mg:

$$\frac{dJ}{dt} = r \times mg, \quad (1.18)$$

the change rate of the angular momentum of a magnetic moment μ is equal to the torque due to the magnetic field:

$$\frac{dJ}{dt} = \mu_0(\mu \times H_{eff}). \quad (1.19)$$

Since the magnetic moment $\boldsymbol{\mu}$ is linked to the angular momentum $\boldsymbol{J}$ by the gyromagnetic ratio γ with the relation (1.2):

$$\frac{1}{\gamma}\frac{d\boldsymbol{\mu}}{dt} = \mu_0(\boldsymbol{\mu} \times \boldsymbol{H_{eff}}). \quad (1.20)$$

Since the magnetization $\boldsymbol{M}$ is the magnetic moment $\boldsymbol{\mu}$ per unit of volume, it is more common to express equation (1.20) with a continuous description of the magnetic moment:

$$\frac{d\boldsymbol{M}}{dt} = \gamma\mu_0\boldsymbol{M} \times \boldsymbol{H_{eff}}. \quad (1.21)$$

This is the so-called Landau-Lifshitz equation. The equation (1.21) implied that the magnetization will precess indefinitely around $\boldsymbol{H}$ with a precessional frequency $\boldsymbol{\omega} = -\gamma\mu_0\boldsymbol{H}$.

Damping

In real magnetic systems, the magnetization $\boldsymbol{M}$ will relax its position parallel to the magnetic field $\boldsymbol{H}$, due to different scattering mechanism (see section 1.4.3). This relaxation effect creates a damping mechanism that tends to minimize the angle between $\boldsymbol{M}$ and $\boldsymbol{H}$. Different way exist to describe the damping by adding a term in the equation (1.21). One way was proposed by Gilbert by describing the damping with a phenomenological viscous-like term[5], proportional to the variation of $\boldsymbol{M}$:

$$\boldsymbol{H_{damp}} = -\eta\frac{d\boldsymbol{M}}{dt}. \quad (1.22)$$

By including this term in the equation (1.21):

$$\frac{d\boldsymbol{M}}{dt} = \gamma\mu_0\boldsymbol{M} \times \left(\boldsymbol{H_{eff}} - \eta\frac{d\boldsymbol{M}}{dt}\right), \quad (1.23)$$

$$\frac{d\boldsymbol{M}}{dt} = \gamma\mu_0\boldsymbol{M} \times \boldsymbol{H_{eff}} + \frac{\alpha}{M_s}\boldsymbol{M} \times \frac{d\boldsymbol{M}}{dt}, \quad (1.24)$$

where $\alpha = -\eta\gamma\mu_0 M_S$ is the Gilbert damping parameters, a dimensionless constant that depends on the material. The equation (1.24) is called the Landau-Lifshitz-Gilbert equation (**LLG**) and is illustrated in Fig.1.3.

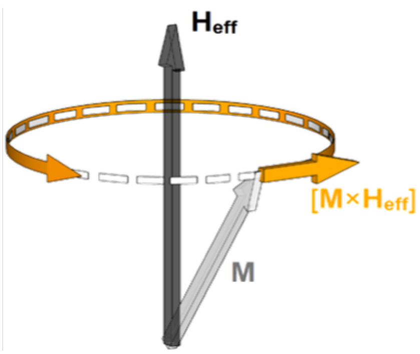

(A)

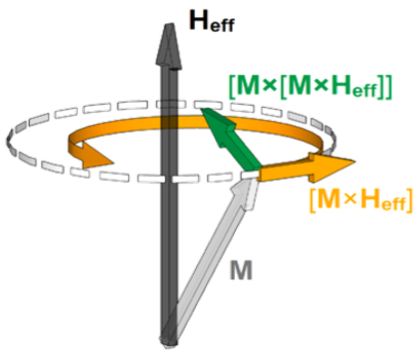

(B)

FIGURE 1.3: Illustration of the LLG equation for an undamped motion (A) and by adding a damping term (green arrow) (B).[6]

1.3 Spin transfer torque

In a standard metal the electric current is unpolarized meaning that 50 % of the electrons have spin-up and 50 % have spin-down. When electrons flow through a thick uniform ferromagnetic material, the majority spins (spin-up) are preferentially transmitted, and the minority spins (spin-down) are preferentially transmitted. Therefore the ferromagnet acts as a spin filter and generates a spin-polarized current. When the spin-polarized current is injected in a standard metal, the current keeps its polarization until a distance called the spin diffusion length due to scattering effects that flip the spin of the electrons (see Fig.1.4).

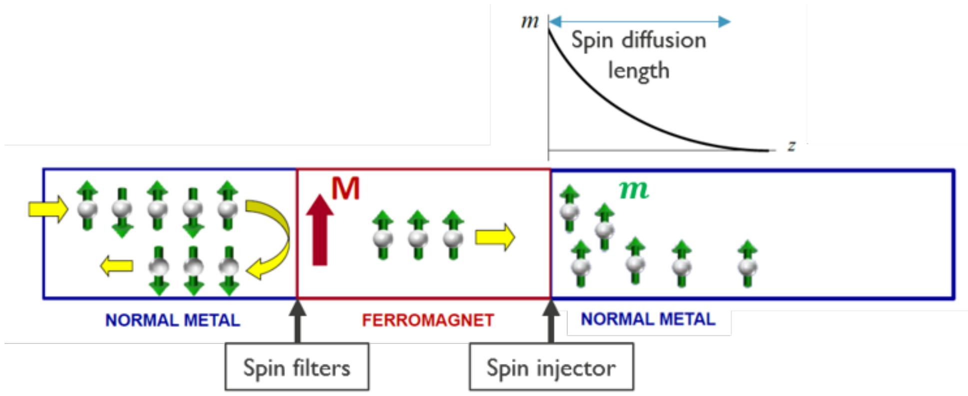

FIGURE 1.4: Illustration of a spin current polarized by a ferromagnet, the spin remains polarized in a normal metal over the spin diffusion length.[7]

As sown in Fig.1.5, if a spin-polarized current is injected in a thin ferromagnetic layer, the electrons can transmit a part of their magnetic moment (m) to the magnetization of the layer (M) by spin transfer torque (STT). Therefore the STT effect can be used to modify the magnetization of thin ferromagnetic layers with an electrical current. Usually, the ferromagnet used to polarized the spin current is called the reference layer, and the ferromagnet subjected to spin transfer is called the free layer (FL).

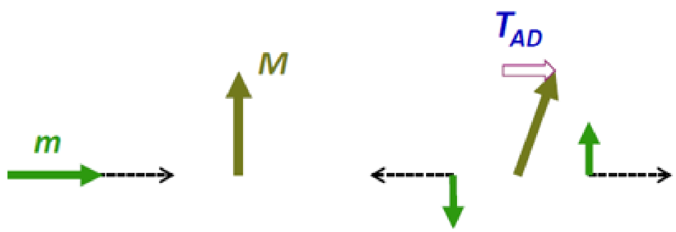

FIGURE 1.5: When a magnetic moment m is injected in a thin ferromagnetic film, a part of the moments is absorbed by the magnetization M. The torque is also called anti-damping torque.[7]

The torque exerted on the magnetization can be expressed by the Slonczewski's spin transfer torque term [8]:

$$\tau = \frac{\chi(J)}{M_s^2}\boldsymbol{M} \times (\boldsymbol{M} \times \boldsymbol{m}), \tag{1.25}$$

where $\boldsymbol{m}$ is the unit vector of the polarized-current. χ represents the strength of the STT effect and depends on the electric current density J. The spin torque induced by the polarized current can be injected in the LLG equation (1.24) to form the so-called Landau-Lifshitz-Gilbert-Slonczewski (LLGS) equation:

$$\frac{d\boldsymbol{M}}{dt} = \gamma\mu_0 \boldsymbol{M} \times \boldsymbol{H}_{eff} + \frac{\alpha}{M_s}\boldsymbol{M} \times \frac{d\boldsymbol{M}}{dt} + \frac{\chi(J)}{M_s^2}\boldsymbol{M} \times (\boldsymbol{M} \times \boldsymbol{m}). \tag{1.26}$$

The Slonczewski's spin transfer torque term is sometimes called anti-damping torque because, following the direction of the moments injected m, the torque can act against the Gilbert damping term as shown in Fig.1.6 (red arrow). Since the torque depends directly on the current density J, when J is low, the torque is not strong enough to overcome the damping torque. When J is high, the torque is larger than the damping torque and the magnetization switches in a direction opposite to the applied field. In an intermediate range of current densities around a critical value J_c, the damping torque and the anti-damping torque compensate each other, and a stable precession is maintained. As shown in Fig.1.7, the magnetization state depends also on the applied filed $\boldsymbol{H}$.

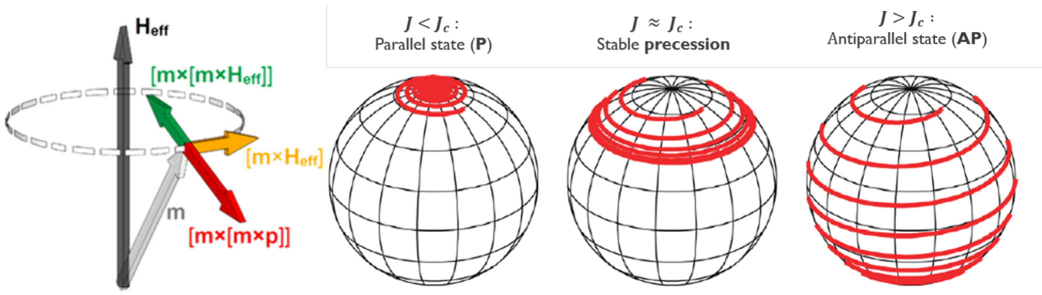

FIGURE 1.6: Illustration of the different magnetization states as a function of the current density J. When J is low the damping motion is dominant. When J is high the STT torque is dominant and the magnetization switch in the direction of the magnetic moments injected. For intermediate value the two torque are equal, and a stable precession is maintained. [6]

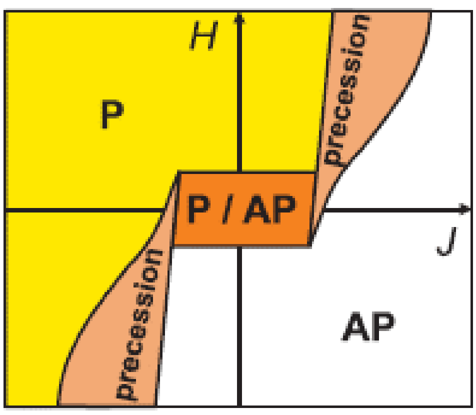

FIGURE 1.7: Diagrame of the magnetization state as function of the current density and as the applied field[9]

1.4 Spin wave

In 1930 Bloch, was the first to introduce the concept of a spin wave[10] by a chain of spins coupled by exchange interaction. His analysis of the small deviation of the spin from their equilibrium shows that these deviations were dynamic and propagate in a magnetic medium. Holstein[11] and Dyson[12] generalized the concept of a spin wave by taking into account the magnetic dipole interaction between the spins and the Zeeman energy.

The dynamics of a single electron cannot be described outside of the quantum mechanics theory, however, a spin wave is not a phenomenon of an isolated electron but of a large ensemble of spin. This macro-spin ensemble allows the description of the spin as a semi-classical object caring a magnetic moment $\bar{\boldsymbol{\mu}}$. This is called the macro-spin approximation where the magnetic moments can still be described by the **LLG** equation (1.24).

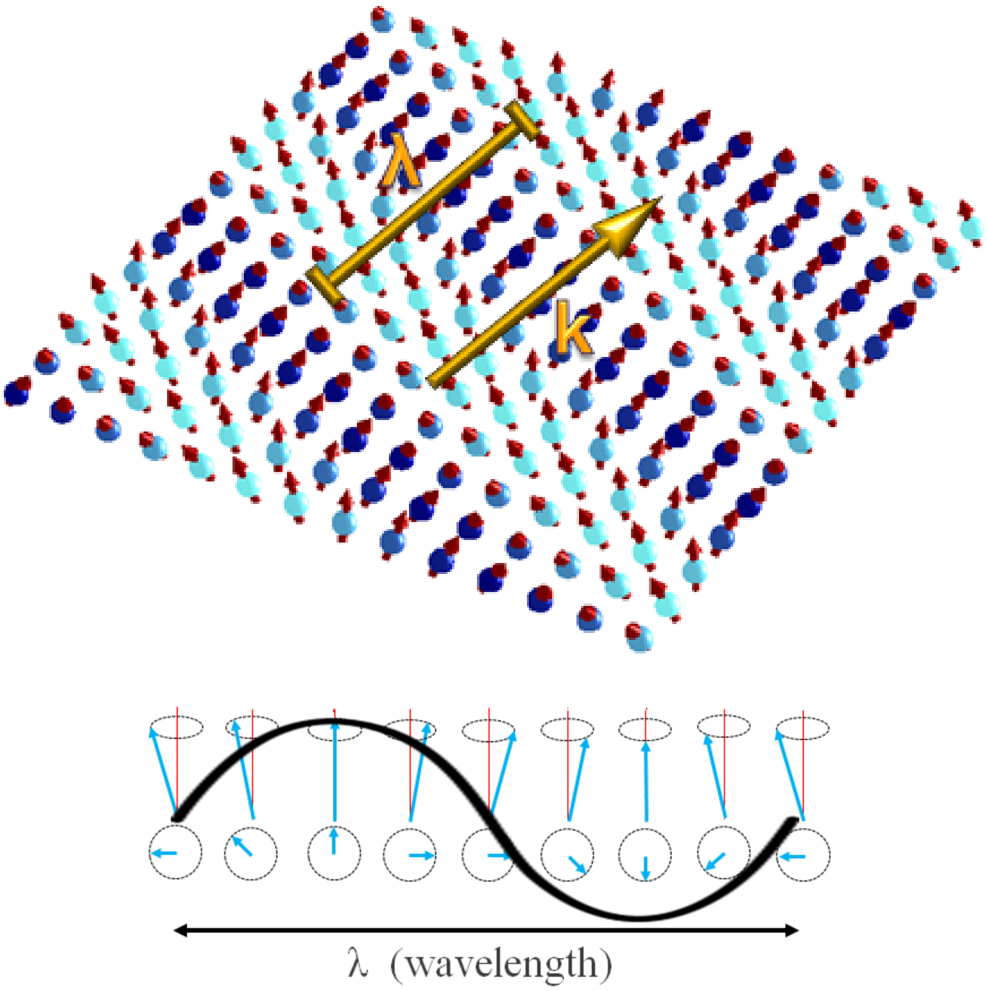

FIGURE 1.8: Illustration of spin waves propagation. The magnetic moments precess at a given frequency but with a phase shift in the direction of the propagation $\boldsymbol{k}$. Two magnetic moments spaced from a distance equal to the wavelength of the wave λ, and in the propagating direction, have the same phase. *Source: F.Ciubotaru*

A spin wave is thus a plane-wave solution of the **LLG** equation (1.24):

$$\boldsymbol{M}(\boldsymbol{r},t) = \boldsymbol{M_0} + \boldsymbol{m}e^{i(\omega t - \boldsymbol{k}\cdot\boldsymbol{r})}, \tag{1.27}$$

where $\boldsymbol{m}$ is the dynamic component of the magnetization. The magnetization precesses with a small-amplitude around its equilibrium, the magnetic saturation M_s. Generally the precession is not uniform in the space but with a phase shift of $\boldsymbol{k}\cdot\boldsymbol{r}$ along the wave vector $\boldsymbol{k}$ as shown on the Fig.1.8. The only exception is when $\boldsymbol{k} = 0$, in this case, all the moments precess with the same phase. The corresponding frequency is called a ferromagnetic resonance (**FMR**).

Since the dynamic perturbation is small compared to the static magnetization $\boldsymbol{M_0}$, $\boldsymbol{M_o}$ can be approximated to the magnetic saturation :

$$|\boldsymbol{m}| \ll |\boldsymbol{M_o}| \approx M_s. \tag{1.28}$$

If $\boldsymbol{M_s}$ is defined as the position vector when the system is at its equilibrium, the equation (1.27) can be written as:

$$\boldsymbol{M}(\boldsymbol{r},t) = \boldsymbol{M_s} + \boldsymbol{m}e^{i(\omega t - \boldsymbol{k}\cdot\boldsymbol{r})}. \tag{1.29}$$

The dispersion relation $\omega(\boldsymbol{k})$ can be calculated by injecting the plane-wave solution (1.29) in the **LLG** equation (1.24). For an unbound 3D ferromagnetic medium, the effective field $\boldsymbol{H_{eff}} = \boldsymbol{H_0} + \boldsymbol{H_d} + \boldsymbol{H_{exch}}$ (see section 1.1) and for a plane wave with a small amplitude as $\boldsymbol{M_0} = \boldsymbol{M_s}$, the exchange field $\boldsymbol{H_{exch}}$ can be expressed as:

$$\boldsymbol{H_{exch}}(\boldsymbol{r},t) = -\lambda_{ex}\Delta\boldsymbol{M}(\boldsymbol{r},t) = -\lambda_{ex}\Delta\left(\boldsymbol{M_s} + \boldsymbol{m}e^{i(\omega t - \boldsymbol{k}\cdot\boldsymbol{r})}\right) = \lambda_{ex}\boldsymbol{k}^2\boldsymbol{m}e^{i(\omega t - \boldsymbol{k}\cdot\boldsymbol{r})} \tag{1.30}$$

By doing so, the dispersion relation $\omega(\boldsymbol{k})$ is given by the Herrings-Kittel formula[13]:

$$\omega(\boldsymbol{k}) = 2\pi f = \gamma\mu_0\sqrt{(H_0 + M_s\lambda_{ex}k^2)\,(H_0 + M_s\lambda_{ex}k^2 + M_s sin^2\theta)}, \tag{1.31}$$

where θ is the angle between the direction of propagation $\boldsymbol{k}$ and the steady-state magnetization $\boldsymbol{M_s}$. Three clear contributions can be identified. H_0 from the Zeeman interaction, $M_s\lambda_{ex}k^2$ from the exchange interaction and $M_s sin^2\theta$ from the dipolar interaction.

Dipolar regime

When the $\boldsymbol{k}$-vector is low, $M_s\lambda_{ex}k^2 \ll \boldsymbol{H_0}$ and the relation (1.32) become:

$$\omega(\boldsymbol{k}) = \gamma\mu_0\sqrt{H_0\,(H_0 + M_s sin^2\theta)}. \tag{1.32}$$

This relation shows that at low $\boldsymbol{k}$, the spin waves mostly depend on the dipolar interaction. The dispersion relation $\omega(\boldsymbol{k})$ is independent of the $\boldsymbol{k}$ vector and depend only on the orientation of propagation compared to the steady-state of magnetization $\boldsymbol{M_s}$. The spin waves in this regime are thus anisotropic. For $\theta = 0$, the frequency $\omega(\boldsymbol{k})$ is:

$$\omega_{||} = 2\pi f_{||} = \gamma\mu_0 H_0 \tag{1.33}$$

and for $\theta = 90°$, $\omega(\boldsymbol{k})$ equal:

$$\omega_{\perp} = 2\pi f_{\perp} = \gamma\mu_0\sqrt{H_0\left(H_0 + M_s\right)}. \tag{1.34}$$

Exchange regime

When $\boldsymbol{k}$ is high, $M_s\lambda_{ex}k^2 \gg M_s sin^2\theta + \boldsymbol{H_0}$ and in this case the relation (1.32) becomes:

$$\omega(\boldsymbol{k}) = \gamma\mu_0(H_0 + M_s\lambda_{ex}k^2). \tag{1.35}$$

At high $\boldsymbol{k}$, the spin waves depend therefore mostly on the exchange interaction. The waves are isotropic (independent of θ) and $\omega(\boldsymbol{k})$ evolves quadratically with $\boldsymbol{k}$.

These two regimes are resumed in Fig.1.9a, $\boldsymbol{\omega(k)}$ firstly evolves constantly in the dipolar regime and then quadratically in the exchange regime.

1.4.1 Magnetostatic modes in thin film

The Herrings-Kittel formula (1.31) is only valid in a bulk ferromagnet. When one dimension is decreased, like in a thin film, the dispersion relation $\omega(\boldsymbol{k})$ strongly depends on the direction of propagation $\boldsymbol{k}$ and the direction of the magnetization $\boldsymbol{M}$ with respect to the geometries of the sample. This is due to the influence of the dipolar field on the magnetization. For this reason, the anisotropy is more important when the wave vector is low because in this regime the dipolar interaction is dominant.

For thin films, Kalinikos and Slavin used the perturbation theory to determine the dependency of the film thickness d, the angle between the magnetic field and the direction of propagation $\boldsymbol{\theta}$ and the angle between the normal of the plane film $\boldsymbol{n}$ and the field $\boldsymbol{\phi}$ on the dispersion relation [14]. The term $sin^2\theta$ in relation (1.31) that describes the dipolar interaction is replaced by a more complex term that depends on d, θ and ϕ:

$$\omega(\boldsymbol{k}) = \gamma\mu_0\sqrt{\left(H_0 + M_s\lambda_{ex}k^2\right)\left(H_0 + M_s\lambda_{ex}k^2 + M_s\boldsymbol{F}(d,\theta,\phi,\boldsymbol{k})\right)}. \tag{1.36}$$

Fig.1.9 compares the dispersion relation (A) for a bulk ferromagnet and for a thin film (B). It clearly shows that in the dipolar regime different mode emerge for a different configuration, the figure shows the tree main mode in a thin film. These modes are called magnetostatic waves (**MSW**) because these waves are a solution a the Maxwell equations in the magnetostatic approximation, meaning that the displacement current generates is negligible. This assumption is possible because, in a ferromagnetic material, the wavelength of spin waves is significantly shorter than the wavelength of an electromagnetic wave.

Since the magnetostatic modes are considered in the dipolar regime, the exchange interaction can be neglected and the relation (1.36) becomes:

$$\omega(\boldsymbol{k}) = \gamma\mu_0\sqrt{H_0\left(H_0 + M_s\boldsymbol{F}(d,\theta,\phi,\boldsymbol{k})\right)}. \tag{1.37}$$

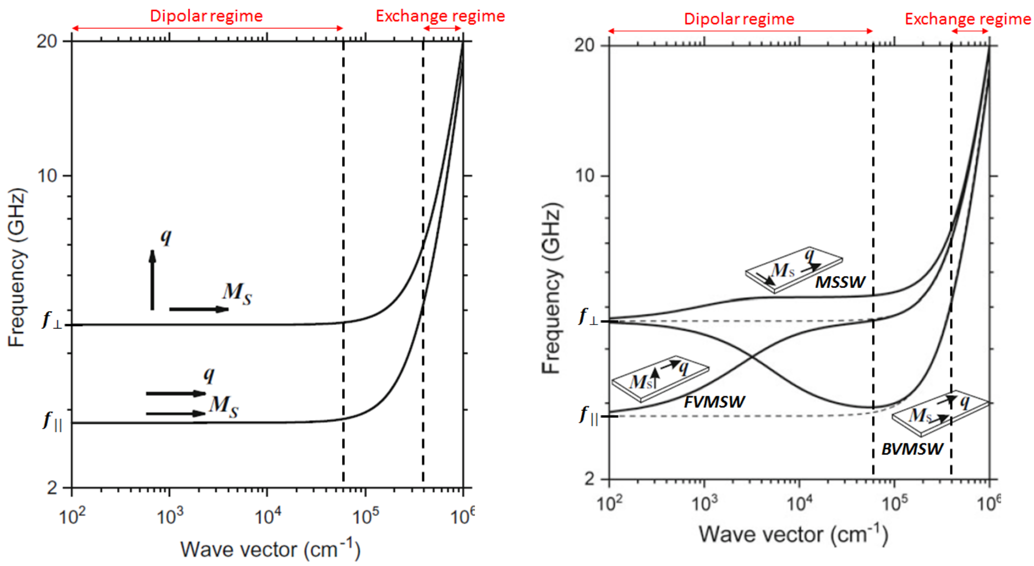

(A) Unbound medium (B) Thin film medium

FIGURE 1.9: Dispersion relation for different magnetostatic modes in unbound medium (A) and in thin film (B). The mode depend on the orientation between the propagation direction ($\boldsymbol{q}$), the magnetization direction (M_s), and the direction of the plane normal. [15]

Magnetostatic surface wave (MSSW)

The Damon-Eshbach mode, also called magnetostatic surface wave corresponds to the mode where $\theta = 90°$ ($\boldsymbol{k} \perp \boldsymbol{H}$) and $\phi = 90°$ ($\boldsymbol{H} \perp \boldsymbol{n}$). For this mode the relation dispersion is given by the relation (1.36):

$$\omega(\boldsymbol{k}) = \gamma\mu_0\sqrt{H_0\left(H_0 + M_s\right) + \frac{M_s^2}{4}\left(1 - e^{-2kd}\right)} \tag{1.38}$$

This mode is called surface mode because of the profile of the amplitude, described by an exponential function with a maximum on one of the interfaces of the film:

$$\boldsymbol{m}(x) = \boldsymbol{m}_0 e^{-kx}, \tag{1.39}$$

where x is the direction of the plane normal. Therefore the propagation is mostly located on the surface of the film. Moreover, the wave is nonreciprocal, the propagation is mostly unidirectional, whereas at the opposite interface the wave propagates in the opposite direction.

Forward volume magnetostatic wave (FVMSW)

In this mode, the field is oriented out-of-plane: $\theta = 90°$ ($\boldsymbol{k} \perp \boldsymbol{H}$) and $\phi = 0°$ ($\boldsymbol{H}||\boldsymbol{n}$). The dispersion relation obtained for this configuration is:

$$\omega(\boldsymbol{k}) = \gamma\mu_0\sqrt{H_0\left(H_0 + M_s\left(1 - \frac{1 - e^{-kd}}{kd}\right)\right)}. \tag{1.40}$$

This mode, like the next one (**BVMSW**), is called volume mode because the waves propagate in all the volume, the distribution of the amplitude follows a cosinusoidal distribution of the thickness of the film.

Backward volume magnetostatic wave (BVMSW)

In the backward volume mode, the field is in the same direction of the wave propagation: $\theta = 0^\circ$ ($\boldsymbol{k}||\boldsymbol{H}$) and with $\phi = 90^\circ$ ($\boldsymbol{H} \perp \boldsymbol{n}$) and the dispersion relation is given by:

$$\omega(\boldsymbol{k}) = \gamma\mu_0\sqrt{H_0\left(H_0 + M_s\frac{1-e^{-\boldsymbol{k}d}}{\boldsymbol{k}d}\right)}. \tag{1.41}$$

This mode has the particularity to have a negative group velocity. This is the consequence of the negative slope of the dispersion relation. Indeed the group velocity is defined as:

$$v_{gr} = \frac{\partial f}{\partial \boldsymbol{k}}. \tag{1.42}$$

In this mode, the group velocity and the phase velocity have therefore an opposite direction of propagation, hence the name backward volume.

1.4.2 Magnon: The particle point of view

Electromagnetic and acoustic waves have their particle equivalent with, respectively the photon and the phonon. Similarly, spin wave has a corpuscular homologous: the magnon. A magnon, the quantum of a spin waves corresponds to the flip of the spin of the electron and for this reason, the spin of a magnon is an integer, meaning that it's a boson. The energy of a magnon is given by:

$$\boldsymbol{E} = \hbar\omega, \tag{1.43}$$

with a momentum:

$$\boldsymbol{p} = \hbar\boldsymbol{k}. \tag{1.44}$$

These equations mean that at the **FMR** frequency ($\boldsymbol{k} = 0$), the system is populated with magnons that possess finite energy without any momentum.

Due to the relaxation effects, each magnon has a characteristic lifetime $\tau(\boldsymbol{k})$. The lifetime is related to the Gilbert damping constant and for one-dimensional waveguides with uniform magnetization, equal to[16]:

$$\tau(\boldsymbol{k}) = \left(2\pi\alpha\omega(\boldsymbol{k})\frac{\partial\omega(\boldsymbol{k})}{\gamma\mu_0\partial\boldsymbol{H_0}}\right). \tag{1.45}$$

The mean free path can, therefore, be expressed as a function of the lifetime:

$$\delta = v_g(\boldsymbol{k}) \cdot \tau(\boldsymbol{k}), \tag{1.46}$$

where v_g is the group velocity, i.e. the velocity of the magnons:

$$v_g = \frac{d\omega(\boldsymbol{k})}{d\boldsymbol{k}}. \tag{1.47}$$

The effective mass of a magnon can be deduced from the curve of the band structure: $1/m^* \propto d^2E/d\boldsymbol{k}^2$. From the dispersion relation (1.31) and the magnon energy (1.43), the effective mass is derived as:

$$\frac{1}{m^*} = \frac{2}{\hbar}\gamma\mu_0 M_s\lambda_{ex}. \tag{1.48}$$

1.4.3 Relaxation mechanism

As seen in section 1.2, in a real magnetic system, the magnetization **M** will relax his position parallel to the magnetic field **H**. This due to different relaxation effects where the energy is redistributed in the magnetic system. In a corpuscular sight, the magnon is scattered by each other or by the phonons in the system and for this reason, have a finite lifetime.

The three main scattering effects are resume in Fig.1.10. The intrinsic spin-spin relaxation (Fig.1.10 (a),(b) and (c)) where the magnons are split or merged and the extrinsic two-magnon scattering due to material imperfection (Fig.1.10 (d)) caused rather by the ionic impurities having a strong spin-orbital coupling or by the inhomogeneities (Fig.1.10 (d)). For this relaxation effect, the energy is redistributed among the magnetic modes. The energy can also be redistributed to the system magnetoelastic interaction and it's called the intrinsic magnon-phonon relaxation or the spin-lattice relaxation. The magnon transfers a part of their energy to the phonon (Fig1.10 (e), (f), (g) and (h). The relative importance of these effects as well as their interdependency, depend on different factor as the structure, the geometry, the effective field, and the magnon population[15].

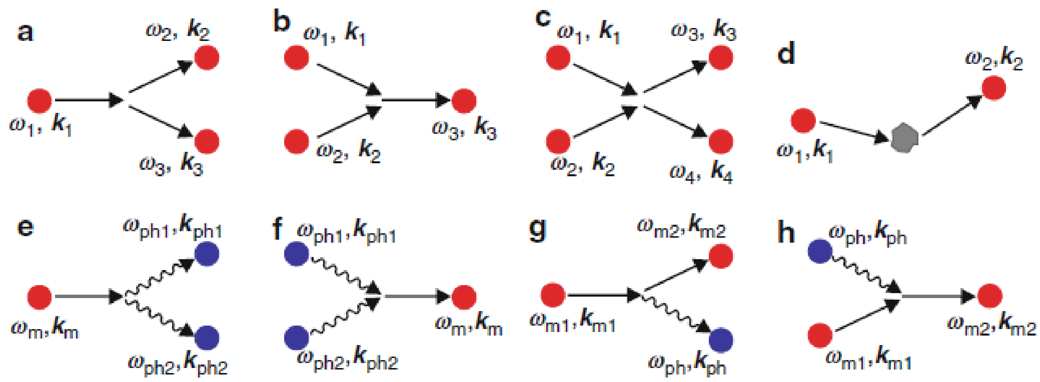

FIGURE 1.10: Magnon scattering processes, the red dot are the magnon and the blue dot are the phonon. (a) Three-magnon scatter. (b) Three-magnon confluence. (c) Four-magnon scatter. (d) Two-magnon scatter. (e) Splitting of one magnon into two phonons. (f) Confluence of two phonons into one magnon. (g) Splitting of one magnon into a second magnon plus a phonon. (h) Confluence of one magnon and one phonon into a second magnon. (g),(h) are Cherenkov processes [4]

Chapter 2

Spin wave devices

Spin waves and their quanta, magnons, are a promising solution for logic computation based on wave interference. The branch is commonly referred to as Magnonics, and it is part of the large family of Spintronic[17]. These devices are based on wave interaction, the magnons carry the information, and the logic function is performed by wave interference. The technology has a potential low power consumption since no electrical charges are involved, and that magnons current doesn't generate joule effect. The footprint of the logic function can be decreased due to the wave-based computing nature allowing a functional scaling down. This chapter introduces the concept of spin wave devices, starting from the context of this technology to their working principle. In the end, devices based on MTJ stacks are details.

2.1 Context and motivation

The unceasing effort of the last decade to scale down the size of the electronics has allowed the exponential evolution of the number of transistor on a chip and maintained Moore's law during 40 years. However, the fundamental limit imposed by physics has drastically reduced its evolution during the last year. In 2016, the International Technology Roadmap for Semiconductors (**ITRS**) had announced the end of Moore's law [18]. For this occasion, the **ITRS** changed his name in International Roadmap for Devices and Systems [19]. Now, the focus is not only on pushing the semiconductors technology to his optimum (*More Moore*) but also rethinking the technology from devices to system level (*More than Moore*).

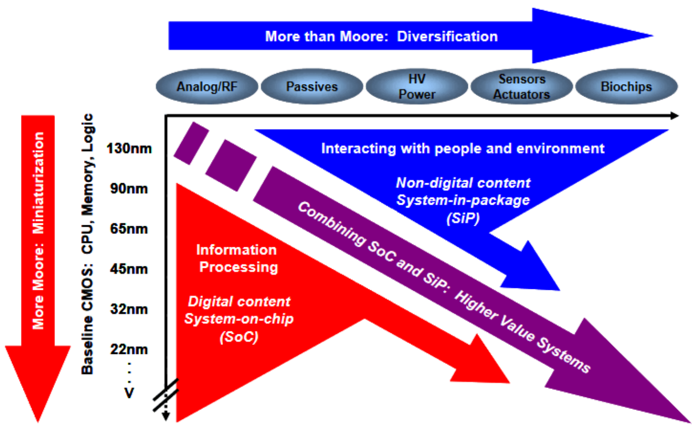

FIGURE 2.1: The International Technology Roadmap for Semiconductors presented in 2011 a dual trend to hence the system's value; textitMore Moore, the miniaturization of the digital functions and *More than Moore*, the functional diversification.[20]

The *More than Moore* strategy refers to the possibility to increase the co-integration and the diversification of the functionality in CMOS circuit [20]. More than the co-integration of the digital technologies developed for the system-on-chip, the aim is the integration and the packaging of many non-digital novel technologies on a single chip. These novel technologies could include optical devices, biotechnology CMOS compatible, molecular electronic analog/RF components, sensors and actuators, spintronics, and so on [21]. In this context, new devices based on spin wave interference have been developed to become potential actors in this novel co-integration.

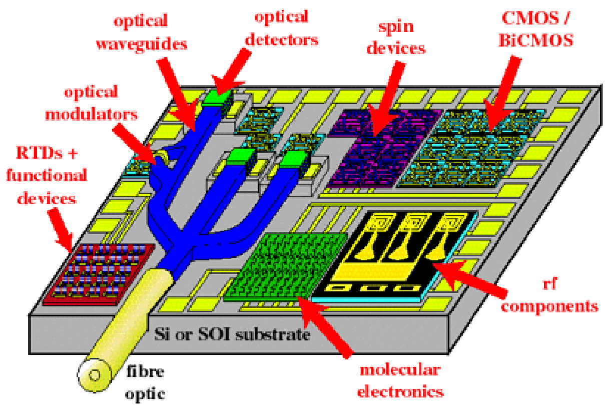

FIGURE 2.2: Illustration of the co-integration of digital and non-digital novel technologies in a single CMOS chip.[21]

One advantage of spin wave technology is the possibility to use higher expressivity logic functions, compared to CMOS, as basic elements such as a majority gate. It is a logic gate with three or an odd number of inputs and one output. The Boolean value of the output corresponds to the Boolean value of the majority inputs. Tab.2.1 shows the truth table of the gate for three inputs. Amaru et al., have shown that the majority gate can be used to build efficient logic circuits and present a great opportunity for logic optimization [22].

Majority function			
input 1	input 2	input 3	output
0	0	0	0
0	0	1	0
0	1	0	0
0	1	1	1
1	0	0	0
1	0	1	1
1	1	0	1
1	1	1	1

TABLE 2.1: Truth table of a majority gate with three input.

This logic function (also called full adder) required 28 CMOS transistors [23], in comparison a spin wave majority gate (SWMG) required three transducers for the input, one for the output, four waveguides and one interconnection. As shown in Fig.2.3, the footprint of the function is not reduced by the scaling down of the single logic element but by the computation mechanism of the SWMG.

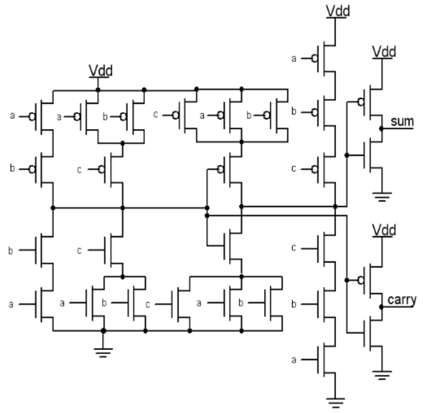

(A)

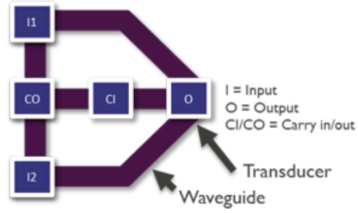

(B)

FIGURE 2.3: Comparison between the footprint of a full adder function using CMOS technology [23] (A) and using spin wave technology (B).

It has been shown that a logic circuit based on spin wave majority gates has theoretically a smaller area than the equivalent circuit in the CMOS 10 *nm* node as well as a lower power consumption even though the clock frequency is smaller [24]. The technology can, therefore, be used for ultra-low power application where the speed and the latency are not critical parameters. Moreover, studies have shown that for some complex algorithm, like microwave signal processing, even the computation speed can present a better efficiency [25][26].

2.2 Spin wave majority gate

Fischer et al. did the first demonstration of SWMG at millimeters scale in 2017 [27]. The gate is a trident shape where the inputs are injected at the three arms, and the interference takes place at the intersection of the waveguides. The Boolean values *'0'* and *'1'* are carried by the phase of the spin waves, respectively 0 and π. The resulting wave (output wave) has the corresponding phase of the majority input wave (see Fig. 2.4).

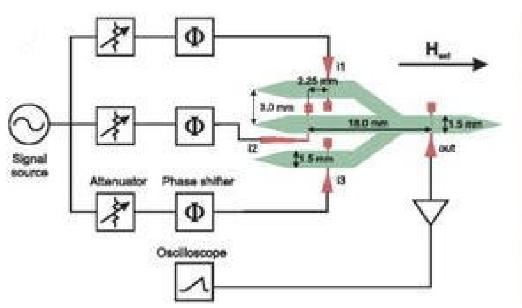

(A)

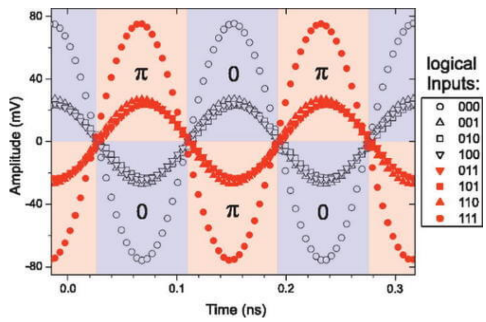

(B)

FIGURE 2.4: First demonstration of SWMG. (A) Scheme of the majority gate. (B) Resulting output detected for the corresponding inputs. [27]

Since the phase detected at the output depends on the propagation distance between the inputs and the output, the wavelength, i.e., operating frequency, has to be matched with the distance. For example, considering only one input connected by a straight waveguide with the output, to emit and detect the same phase, the corresponding frequency must have a $\boldsymbol{k}$-vector equal to:

$$\boldsymbol{k} = \frac{2\pi n}{r} \qquad \text{with} \qquad n = 1, 2, 3..., \tag{2.1}$$

where r is the distance between the output and input. Thus, for the same device, a signal with different frequency components can be used at the same time enabling parallel computing.

Nevertheless, in the trident configuration, the waves are reflected at the bending of the waveguides when a change of direction occurs, and for this reason, limits the frequency that can be used. To solve this issue an in-line configuration, where all the inputs and the output are aligned on a unique straight waveguide, can be used. This configuration allows frequency multiplexing (operation with multiple frequencies at the same times). Furthermore, it provides reconfigurability, thanks to the symmetry of the structure. Each transducer can be interchangeably used as input or output, enhancing the room for circuit optimization. Moreover, this design simplified the fabrication process.

Nonetheless, the trident or the in-line gate still make a distinction between weak/strong output. The signal of a weak output (corresponding for example to an input configuration: $\pi 0 \pi$) and a strong output (input: $\pi\pi\pi$) presents the same phase (as it should be) but with a difference in signal amplitude as shown on Fig.2.5. This distinction makes the cascability of multiple gates more difficult, even though it has been shown that weak/strong distinction can be used for pattern recognition and non-Boolean computation[28].

In 2018, Ciobotaru et al. present the first demonstration of an in-line SWMG at the microscale [29]. The waveguide is made of $CoFeB$, 30 nm thick and 5 μm wide, and the inductive antenna reach a width of 500 nm. The full truth table of the majority function has been proved as well as the reconfigurability. The energy consumption is estimated on average as 7.6 times lower than the 10 nm node of the CMOS technology.

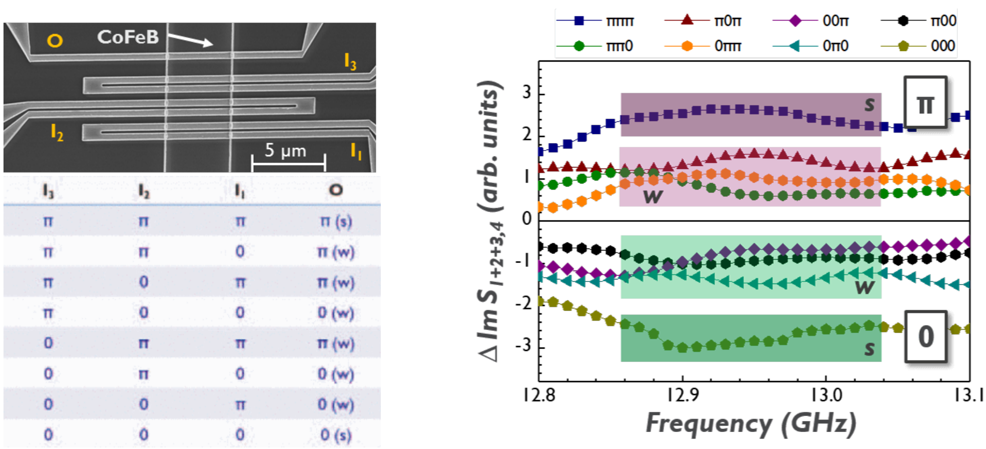

I_3	I_2	I_1	O
π	π	π	π (s)
π	π	0	π (w)
π	0	π	π (w)
π	0	0	0 (w)
0	π	π	π (w)
0	π	0	0 (w)
0	0	π	0 (w)
0	0	0	0 (s)

FIGURE 2.5: In-line SWMG. On the top left, SEM picture of the gate. On the bottom left the truth table of the majority function. On the right, the output signal shows a clear, distinguishable state over a frequency band of 150 Mz. The gate makes a distinction between weak (W) and strong (S) output. [29]

2.2.1 Transducers

The transducers are the interfaces between the electronic and the magnetic domains and are, therefore, critical for the co-integration of spin wave networks in CMOS technology. The power efficiency of the transduction is of fundamental importance to keep low power consumption, so their study, as well as a proposal of new mechanisms, has got increased interest. The two transducers of interest for this thesis are presented here.

Antenna

The antenna transducers are induction based mechanisms. An RF current is injected in a metallic wire perpendicular to the waveguide and generates a magnetic field by the Oersted's law inside the magnetic waveguide. The field produced applies a torque on the magnetization, forcing the magnetic moment out of their equilibrium position. The precession of the magnetic moments with a frequency equal to the frequency of the electrical current generates a propagating spin wave.

Fig.2.6 illustrates two spin wave devices with one input and one output using antennas with the applied external magnetic field perpendicular to the waveguide (MSSW mode) and parallel (BVMSW mode). In both cases, the antenna creates on oscillating Oersted field in the y and z directions (considering that the current flows in the x direction). In the MSSW mode, the magnetic moments are aligned in the x direction due to the external field, and the Oersted field contributes to the precession of the moment in both directions y and z. In the BVMSW mode, the magnetic moments are aligned in the z direction. Therefore, only the y component of the Oersted field contributes to the precession of the spin (in this mode the spin precess in the xy plane). For these reasons, the intensity of the signal detected is higher in the MSSW due to a higher amplitude of the generated spin waves.

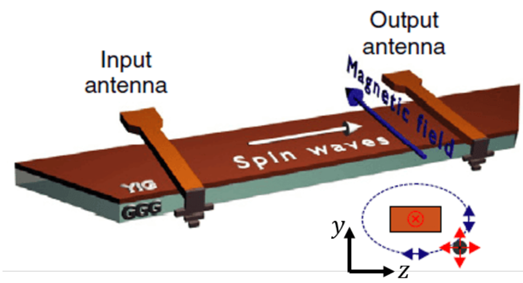

(A) MSSW

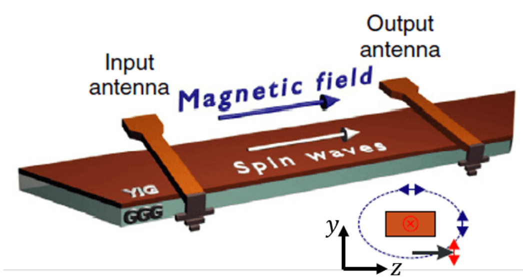

(B) BVMSW

FIGURE 2.6: Schematic representation of spin wave devices based on antenna transducers for the mode MSSW (A) and BVMSW (B). The current flow in the x direction and the wave propagated in the z direction. In MSSW mode, the efficiency of the antenna is better due to the orientation of the magnetic moment in the waveguide. [30]

The excitation and detection by an inductive antenna is a well-known mechanism, allowing an efficient emission over a broad range of frequencies only limited by the size of the antenna (the minimum wavelength that can be exited correspond to the width of the antenna). However, this type of transducers suffers substantial power inefficiency when scaled down at sub-micron dimension. The mechanism, thanks also to the simple fabrication, is heavily used to characterize the spin wave properties in different materials.

STNO

Other alternatives are investigated to overcome the limitation of the scaling down of the antenna transducers. The transducer of interest in this study is based on spin transfer torque. As explained in section 1.3, a spin current can be used to overcome the damping torque, the moment injected in the free layer applies a torque on the magnetization to maintain a stable precession.

The formation of stable precession by spin transfer torque has been used to develop nano-oscillators called spin torque nano-oscillators (STNO) for active microwave devices. A DC current is injected in an magnetic tunnel junction (MTJ), and the spin-polarized current maintains a steady precession of the magnetization in the free layer. An oscillating voltage is measured via tunnel magnetoresistance (TMR) between the junction [1].

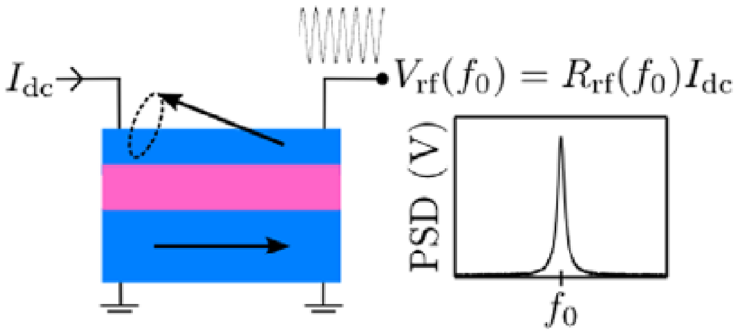

FIGURE 2.7: STNO operating principle. A current is injected in an MTJ, by STT effect the spin current maintains a steady precession of the magnetization. The precession of the magnetization generated an oscillating output voltage by TMR.[32]

Theoretical work has predicted that STNO can be used to excite spin waves. Experimental observation of spin wave generated by STNO has been performed in a thin film of Permalloy [33] and a magnetic waveguide of CoFeB [34]. Magnons are detected by Brillouin light scattering (BLS) microscopy, a spectroscopy technique allowing the detection of spin waves by elastic scattering between photons and magnons.

For the integration of magnonic devices on CMOS chips, it is essential to implement a complete device, that means with electrical/magnon signals conversion for the emission and the detection. Up to date, no complete spin wave device based on STNO transducers has been reported. In the previous studies, the detection is made by BLS microscopy (i.e., detection with electromagnetic wave signal).

STNO transducers are based on tunneling junctions and can be patterned in a pillar shape above the waveguide, improving the possibility for the scale down. Furthermore, the efficiency of spin transfer torque is related to the current density that increases when the pillar area decreases (for the same current), therefore, the performance can be enhanced with the scaling down. Moreover, IMEC have already developed a full 300 *mm* process for similar devices in its semi-industrial cleanroom. Therefore, after a first characterization at the lab level, the materials could be integrated into the line with few modifications to process steps.

[1]Further information can be found in *Theory of Microwave Generation by Spin-Polarized Current* [31]

2.3 Spin wave devices on orthogonal MTJ

The purpose of this thesis is the study of a specific orthogonal MTJ stack for spin wave devices; the stack is called orthogonal due to the fact that the magnetization of the fixed layer is pinned out-of-plane and the free layer has a magnetization in-plane. The material characterization is done using antenna devices, and at the same time, the development of the process to fabricate in the laboratory STNO devices with extended waveguide is started. This mechanism is combined with antennas for detection.

Antenna devices

The first type of device processed is based on antenna transducers on the top of the MTJ stack (see Fig.2.8). The purpose is to study the spin wave propagation in the stack. This includes the study of propagation in the free layer but also the influence of the fixed layer above as well as the possible detection of other modes in the fixed layer.

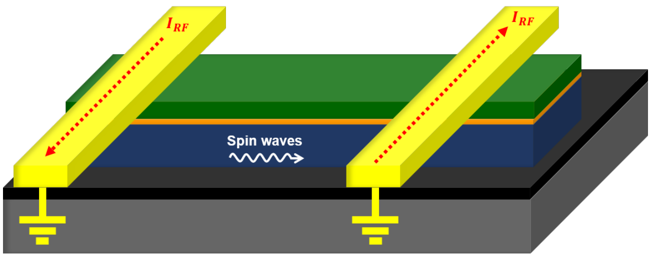

FIGURE 2.8: Antenna device aims to study the spin waves propagation in the MTJ stack using antenna transducers (in yellow). In blue, the free layer; in green, the fixed layer; and in orange, the junction.

To fully characterize the propagation, devices with different parameters variation are fabricated, as shown in Fig.2.9. The parameters of interest are the waveguide width W, the distance of propagation P (i.e., the gap between the antenna) and the width of the antenna A, as well as the thickness of the free layer d.

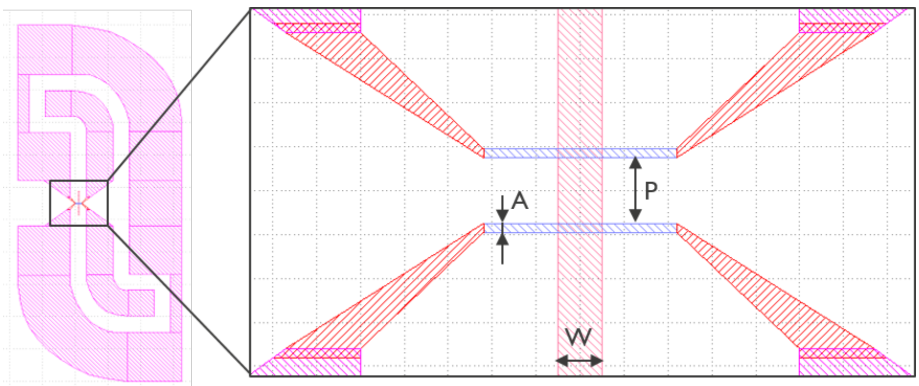

FIGURE 2.9: Design of the antenna devices, the antenna A are in blue and the waveguide W is in orange.

The active area of the device, including only the waveguide and the antenna, measure is around 20 μm × 10 μm. The full device, including the contact electrodes for the microprobe, measures 500 μm × 1000 μm. Since the external field and the microprobe are fixed on the RF setup, the contact electrodes are designed in an S-shape in order to connect the device with the external field transversal to the waveguide (MSSW mode) and parallel (BVMSW mode).

STNO devices

The targeted STNO device is based on transducer using an MTJ to emit spin waves by STT effect. The polarized layer is perpendicular to the plane, and the free layer is in-plane. The spin current is therefore 90° oriented with respect to the free layer magnetization, leading to a maximum torque as shown by the formula: $\tau \propto \chi(J)(\boldsymbol{M} \times \boldsymbol{m})$ (see section 1.3). The size of the pillar is patterned down to 100 nm, to maximize the efficiency by increasing the current density J.The detection is performed by an antenna since it is a well-known transducer, and is more suitable to characterize the emission by STT.

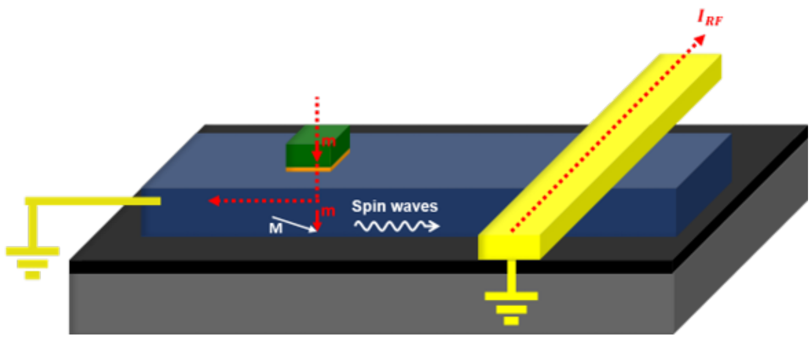

FIGURE 2.10: STNO device. The pillar injects a spin-polarize current in the free layer by a 90° orientation. The signal is pick-up by an antenna transducer.

The same parameters variation as before are introduced to characterize the propagation together with the variation of the pillar size (CD). Besides the standard vehicle made of one STNO transducer for the emission and one antenna for the detection (Fig.2.11a), a majority gate with three STNO transducers for the inputs and one antenna for the output is also designed (Fig.2.11b).

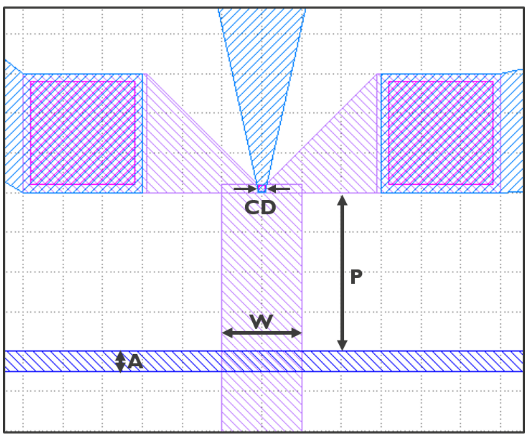

(A) Standard STNO vehicle

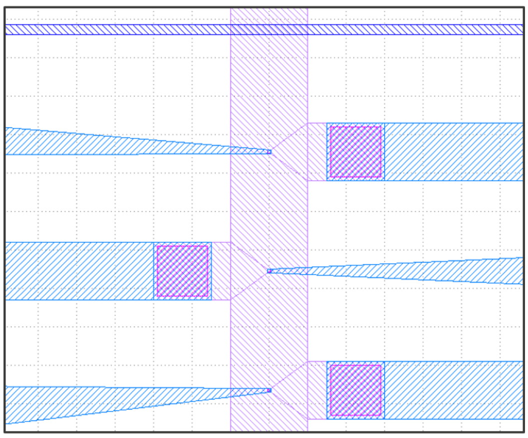

(B) STNO majority gate

FIGURE 2.11: Design of the STNO devices. The emission is made by an MTJ pillar with a size CD, and the signal is detected by antenna A.

Chapter 3

Material and Fabrication process

3.1 Material characterization

The process of the devices start with a blank 300 *mm* wafer (i.e., without structure) composed of a multilayers stack, made of three principal magnetic part; the hard layer made of a synthetic antiferromagnet (SAF), the reference layer (RL) and the free layer (FL) on the top the substrate.

The SAF composing the hard layer is a multilayers structure alternating several times a thin layer (below 1 *nm*) of cobalt and platinum for a total thickness of 11 *nm*. On the top of the SAF, a thick capping layer of ruthenium (7 *nm*) protect the stack against the oxidation. Moreover, the oxide of ruthenium is conductive, allowing the connection with electrical contact even is the structure is oxidized. The reference layer, a Cobalt/Iron/Boron alloy ($CoFeB$), 1.1 *nm* thin, is separated with the hard layers by a thin layer of Tungsten (0.3 *nm*). The reference layer and the free layer below are spaced by an oxide layer (MgO) of 1 *nm* acting as a tunneling junction.

The stack is deposit on a substrate of $SiO_x(300nm)/Si$ on top of an adhesion layer made of Tantalum (0.2 *nm*). The layers are deposited by sputtering deposition inside the semi-industrial line of IMEC. For the studies, three wafers of 300 *mm* with each a different thickness of the free layer (2.5 *nm*, 5 *nm*, and 10 *nm*) are used.

The reference layer with a magnetization out-of-plane is used to inject a polarised current by tunneling effect through the oxide layer and generate a torque on the in-plane free layer magnetization. The SAF is optimized to compensate the stray field inside the free layer.

3.1.1 Static magnetic properties

The three main parts of the stack have specific proprieties. The synthetic anti-ferromagnet, also called the hard layers, is an alternation of two non-ferromagnetic material hence the name synthetic. Due to the interfacial effect between the two layers, they polarised their magnetization out-of-plane spontaneously but with opposite direction hence the name anti-ferromagnet[1]. These layers create a stray field, optimized to cancel the stray field created by the reference layers inside the free layer. The net magnetization in this part is, therefore, out-of-plane.

The thin ferromagnetic material used for the reference layer has usually, like most of the thin ferromagnetic material, an easy axis in the plane due to the shape anisotropy (see section 4.3.4). But due to a strong coupling at the interface with the $Mg0$ layer, the reference layer has its magnetization aligned out-of-plane. The effect called perpendicular magnetic anisotropy (PMA) is a strong coupling active over a

[1] More precisely, Co is ferromagnetic but with a negligible effect for these thickness. The magnetic order of the SAF originates from a strong spin-orbit coupling at the Pt/Co interface

short distance, typically for a layer around 1 nm, that keep the polarization out-of-plane.

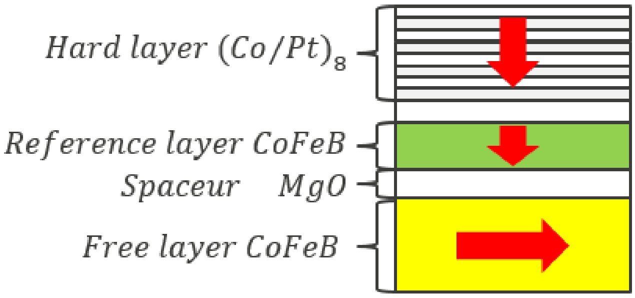

FIGURE 3.1: Magnetic proprieties of the stack. The SAF has a spontaneous magnetization out-of-plane due to the interface coupling Pt/Co, and the reference layer is also out-of-plane due to the interface coupling $Mg0/CoFeB$. The free layer is in-plane due to the dominant shape anisotropy compare to the perpendicular magnetic anisotropy (PMA).

Finally, the free layer is made of the same ferromagnetic material than the reference layer. However, this layer is thicker (from 2.5 nm to 10 nm depending on the wafer). For this thickness, the PMA is not strong enough to keep the magnetization perpendicular, and the magnetization tends to go in-plane. These three magnetic behaviors are illustrated in Fig. 3.1.

Vibrating-sample magnetometer

The behavior described in the previous section can be measured and quantified by a vibrating-sample magnetometer (VSM). This instrument is used to measure the magnetic properties of a sample. More precisely, this technique measured the magnetic response of a sample under an external field. It is, therefore, possible to extract the coercive field and the value of the magnetic saturation with this instrument.

The sample is magnetized in a uniform magnetic field, and it is sinusoidally vibrated. The movement induces a change in the magnetic flux ϕ and by the Faraday' law, generates a voltage inside two pickup coil mounted on the instrument:

$$V_{coil} = -\frac{\partial \phi}{\partial t}. \tag{3.1}$$

Between two coils, the magnetic flux ϕ is proportional to the magnetic flux density $\boldsymbol{B}$. Therefore, the voltage is proportional to the change of magnetic flux density $\boldsymbol{B}$. For a constant Field $\boldsymbol{H_0}$:

$$\frac{\partial \boldsymbol{B}}{\partial t} = \frac{\partial}{\partial t}\left(\mu_0(\boldsymbol{H_0} + \boldsymbol{M})\right) = \mu_0 \frac{\partial \boldsymbol{M}}{\partial t}. \tag{3.2}$$

Therefore, the voltage induces in the coils depends only on the magnetization $\boldsymbol{M}$ and not on the external field $\boldsymbol{H_0}$. The voltage measured by the pick-up coil is used to deduce the total magnetic moment of the sample in emu; the value of the magnetization (emu/cm^3) is found by dividing the magnetic volume of the material. The VSM instrument used for the characterization can measure the magnetization with high precision and for an applied field up to 25 000 Oersted (2.5 T).

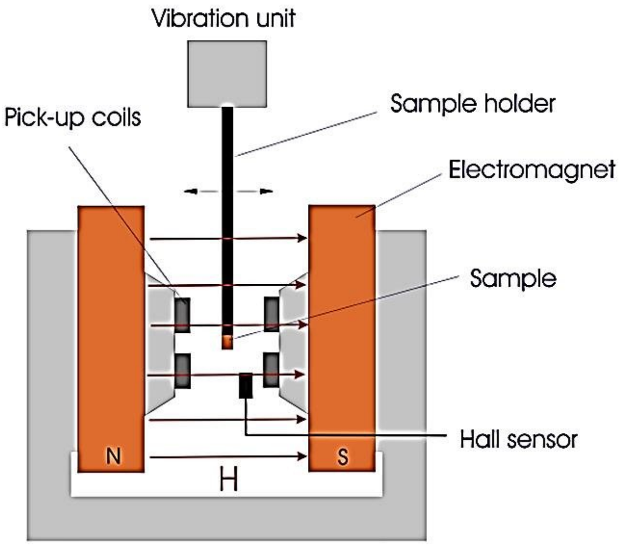

FIGURE 3.2: Schematic representation of a VSM instrument. The sample is vibrated between two electromagnets. Two pick-up coil measures an electrical current generated by induction. The current is related to the sample magnetization. [35]

In the present case, nevertheless, the measurement is performed on a multilayer stack. The measurement aims to characterize the behavior of the full stack, that depends on the thickness of the different layers, and compare the magnetic proprieties when the thickness of the free layer changes. Therefore, it makes more sense to compare the magnetic moment per unit area (emu/cm^2) rather than by unit volume.

Furthermore, the VSM measures the total magnetic moment, meaning that the magnetic moment of the substrate (SiO_x/Si) is also measured. The substrate has a diamagnetic behavior; consequently, the magnetization is linear with the magnetic field, and the magnetic susceptibility is constant:

$$M_{sub} = \chi_{sub} H, \tag{3.3}$$

where H is the external field applied by the VSM and χ_{sub} the magnetic susceptibility of the substrate. Since the total magnetic moment is equal to:

$$M_{tot}(H) = M_{stack}(H) + M_{sub}(H) = M_{stack}(H) + \chi_{sub} H, \tag{3.4}$$

it is possible to remove the diamagnetic component in the signal to keep only the magnetic moment of the stack:

$$M_{stack} = M_{tot} - \chi_{sub} H. \tag{3.5}$$

Due to the high anisotropy of the layers in the stack (coming from the shape and interface anisotropy), the evolution of the magnetization with the field is different when the field is applied perpendicularly to the plane layer (out-of-plane measure) or when the field is applied parallel to the plane (in-plane measure). This two type of measurements provides different information about the magnetic proprieties.

Out-of-plane field measurement

Fig.3.3 shows the hysteresis loop of the stack for an applied field perpendicular to the plane. The curves correspond to the three different stacks with different free layer thickness d.

At high fields, the full stack is saturated out of the plane. When the field decreases, the magnetization of the free layer goes back, almost linearly with the field, in-plane. When the field increases in the other direction, the magnetization of the perpendicular layers switch (i.e., direct change of sign with the same amplitude) after a given coercive field H_c. The magnetization of the free layer progressively tilts with the filed in the upright position until the full saturation of the stack at high field.

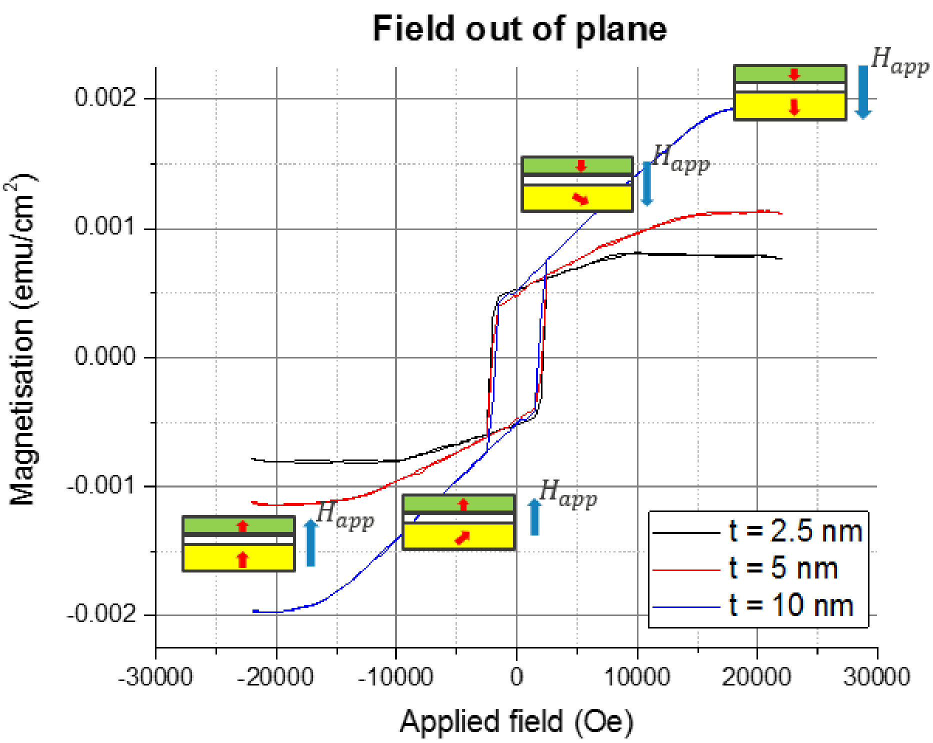

FIGURE 3.3: Magnetic measurement with external field out-of-plane. The red arrows indicate the direction of magnetization inside the layers. In yellow, the free layer and in green, the perpendicular layers.

The coercive field H_c corresponds to the hysteresis behavior of the perpendicular layers. As expected, H_c doesn't change for the three stacks since these layers are the same for every wafer. The slope of the curves before the saturation is proportional to their respective free layer thickness d. It is consistent with the fact that these curves describe the change of the magnetic moment per unit area M^{FL}_{surf} inside the free layer:

$$M^{FL}_{surf} = \chi^{FL} H_{app} d, \tag{3.6}$$

and it is, therefore, possible to extract the magnetic susceptibility of the free layer.

In-plane field measurement

Fig.3.4 shows the hysteresis loop of the stack when the field is parallel to the plane for the three different stacks. At high fields, all the layers are saturated in-plane. In contrary to the out of plane measurement, when the field decrease, it's the perpendiculars layers that tend to go back in their equilibrium position (out-of-plane). At zero field, these layers are perpendicular to the plane, and the free layers switch in the opposite direction. When the field increases in the opposite direction, the perpendicular layers are progressively saturated in-plane, until the full saturation.

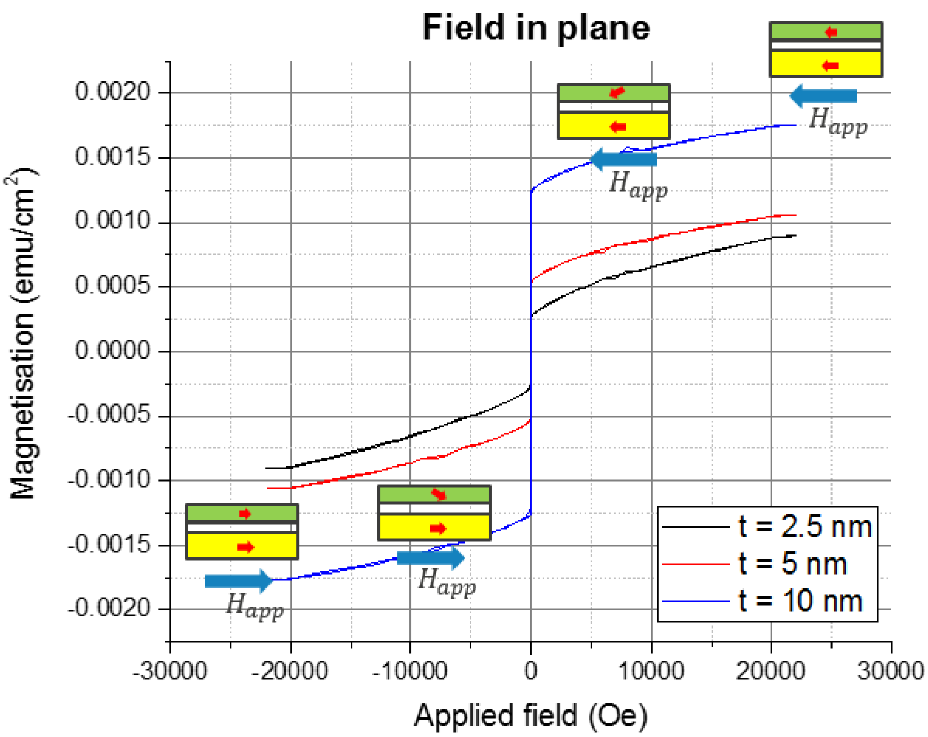

FIGURE 3.4: Magnetic measurement with external field in-plane. The red arrows indicate the direction of magnetization inside the layers. In yellow, the free layer and in green, the perpendicular layers.

In this case, the curves present a low coercive field. The free layer directly switches after passing by zero fields with a change of magnetic moment per unit area M_{surf} proportional to his respective thickness. The free layer instantly saturates in-plane after zero fields, and the evolution of M_{surf} is therefore linked by the magnetic saturation (emu/cm^3) of the free layer M_s^{FL} by:

$$M_s^{FL} = \frac{M_{surf}(H = 0)}{d}. \quad (3.7)$$

The slope of the curve, after zero field, describes the evolution of the magnetization of the perpendicular layers. Since these layers are the have the for every sample, the slopes are also the same for the three curves.

Layers proprieties

These measurements give useful information about the proprieties of the different layers. First, the measurement doesn't show any distinguishable behavior between the perpendicular layers. No significant element can indicate that the SAF and the reference layer switch at a different coercive field or saturate differently. The SAF and the reference layers are therefore probably strongly coupled. For this reason, these layers can be considered as a uniform magnetic system and will be referred to the perpendicular layers (PLs) in the rest of this thesis. However, the properties of the free layer and the perpendicular layer can be easily decoupled.

The free layer shows the following proprieties:

- $M_s^{FL} \approx 1250\ (emu/cm^3)$
- $\chi^{FL} \approx 0.05$
- $H_c^{FL} \approx 20\ (Oe)$

These values are expected for a thick layer of CoFeB without perpendicular magnetic anisotropy.

In the same way, it is possible to extract the magnetic proprieties of the perpendicular layer. Notice that on the contrary of the free layer, this layer is composed of multiple material and only describe a global behavior:

- $M_s^{PL} \approx 425\ (emu/cm^3)$
- $\chi^{PL} \approx 0.0875$
- $H_c^{PL} \approx 1700\ (Oe)$

To conclude, the free layer shows the characteristic of soft magnetic material; the remanence is low with a higher magnetic saturation M_s compared to the perpendicular layer. On the other hand, the perpendicular layer has the characteristic of a hard magnetic material due to the higher coercive field. The susceptibility is also lower in the perpendicular layer, meaning that it requires a higher filed to change the magnetization.

Therefore, this stack is suitable for the target application by spin transfer torque. The fixed layer (here the perpendicular layers) has to keep a fixed magnetization to inject a spin current. The spin current must easily manipulate the free layer to generate a fast dynamic of the magnetization and the emission of spin waves.

3.2 Antenna devices process flow

In this section, the main step of the fabrication of the first generation of devices referred as antenna devices will be succinctly described. As a reminder, these devices are made of two inductive antennas patterned on a magnetic waveguide. Fig.3.5 presents a schematic representation of the main step of the fabrication

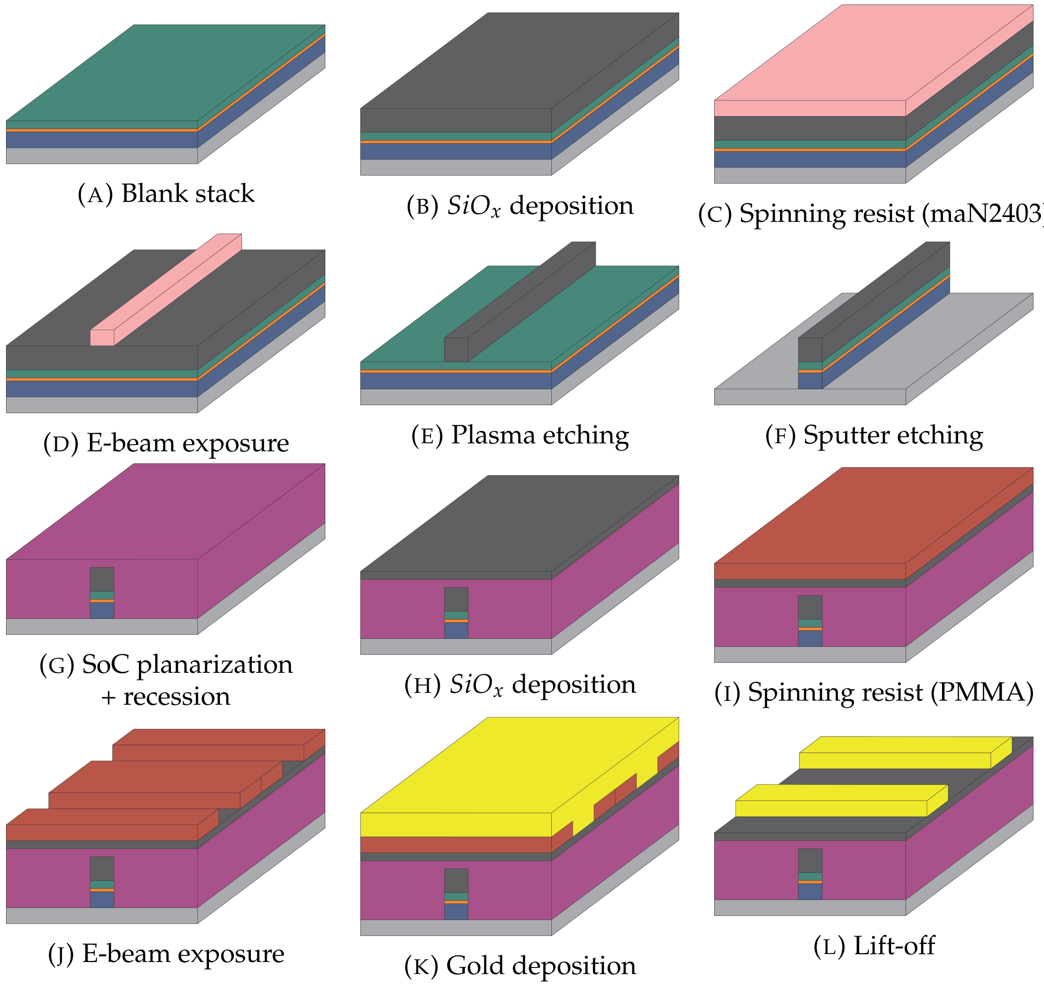

(A) Blank stack
(B) SiO_x deposition
(C) Spinning resist (maN2403)
(D) E-beam exposure
(E) Plasma etching
(F) Sputter etching
(G) SoC planarization + recession
(H) SiO_x deposition
(I) Spinning resist (PMMA)
(J) E-beam exposure
(K) Gold deposition
(L) Lift-off

FIGURE 3.5: Antenna devices process flow. Starting from the magnetic stack (A), 60 *nm* of SiO_x is deposited by sputtering (B). A negative resist of maN2403 is spun (200 *nm*) (C) and after an E-beam exposure for the waveguide, the resist is developed (D). The SiO_x hard mask is defined by plasma etching (E). The waveguide is etched with an ion miller (F). A thick layer of SoC is spun, and the SoC is recessed by plasma etching to planarized the surface (G). Another 30 *nm* of SiO_x is deposited by sputtering (H). After the spinning of PMMA resist (I), a second E-beam exposure is performed for the pattering of the antennas (J). A 10/100 *nm* layer of Ti/Au is sputtered (K). After a lift-off step, the antennas are defined(L).

3.2.1 Magnetic waveguide definition

The waveguide is defined by etching the full stack with a hard mask made of SiO_x. Starting from the stack presented in the previous section, a 60 nm layer of SiO_x is deposited on the sample. A negative resist of maN2403, 200nm thick, is spun above the SiO_x layer. The resist is exposed by electronic lithography defining the waveguide area. The resit is removed everywhere else than the exposed area and will act as a protective layer during the etching of the SiO_x (See Fig.3.5a-d).

The SiO_x hard mask is etched by a CF_4 plasma. After the removal of the remaining resist, the full stack is etched by ion milling, except where the SiO_x protect the surface (See Fig.3.5e,d).

In addition to its role as a mask, the layers of SiO_x remaining above the waveguide acts as an insulation layer between the waveguide and the antennas.

3.2.2 Planarization

Before patterning the gold antennas on the waveguide, the whole sample has to be planarized to have a flat surface. Otherwise, the shape of the antenna will follow the contour of the waveguide, as shown in Fig.3.6b. Since the free layer is conductive, this can cause a leak of the current through the waveguide. Furthermore, the antenna will surround the waveguide, creating a lateral component on the oscillating Oersted field inside the waveguide. Moreover, a change of the current direction formed by the corner increase the reflection of the RF signal inside the antenna and, therefore, increase the noise during the detection. The gold on the sidewalls can also be much thinner, increasing the resistance of the antennas or even create a short-circuit.

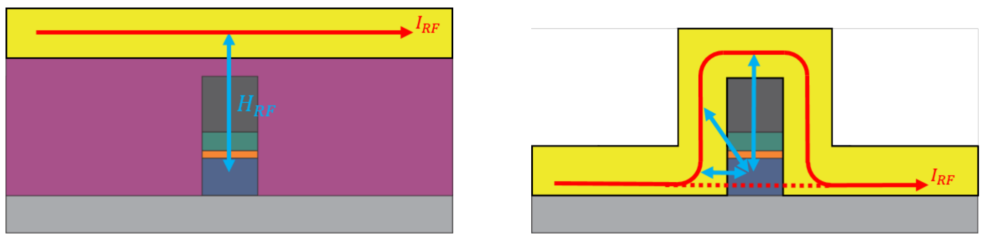

(A) (B)

FIGURE 3.6: Profile of the antennas with and without planarization. When the antenna is flat (A), the Oersted field generated is uniform inside the waveguide. When the antenna follow the shape of the waveguide (B), the current is short through the waveguide.

To planarize the sample, a thick layer of SoC is spun. Since the thickness of the SoC layer is higher than the structure beneath the SoC, the top of the surface present only a large and thin bump (see Fig.3.7a). A recession of this layer is made by plasma etching. The etching stop just before the $Si0_x$ layer in order to reduce the distance between the antenna and the waveguide as much as possible. After the etching, a flat surface remains above the structure (See Fig.3.7b).

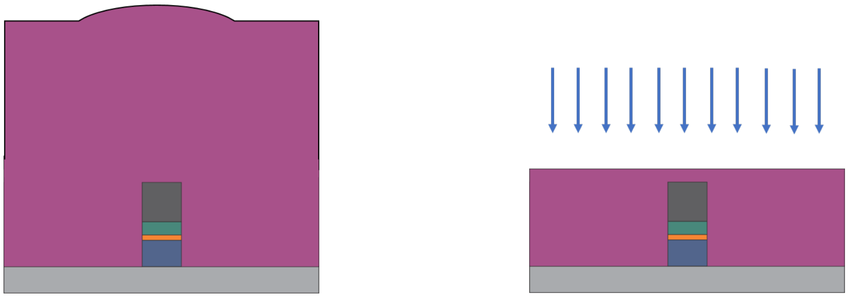

(A) Planarization (B) Recession

FIGURE 3.7: (A) spinning of a thick *SoC* layer, the waveguide create a bump in the *SoC* profile. (B) After a recession of the *SoC* layer by plasma etching, the surface above the waveguide is almost flat.

3.2.3 Antenna deposition

The last part of the process consists of the antennas patterning, perpendicularly to the waveguide. To asses good insulation, an additional SiO_x layer of 30 nm is deposited on the SoC and a positive resist of 400 nm made of PMMA is spun above the previous layer.

The second electronic lithography and the development removed the resist on the areas exposed, as shown in Fig.**??**. These areas are filled with 100 nm thick gold via sputtering deposition (Fig.3.8b). Notice that before the gold deposition, a thin layer of 10 nm of titanium is deposit to grant a good adhesion of the gold antenna.

The final step is performed by a lift-off; the sample is put in acetone over one night to remove the resist. When the resist is removed, the gold deposited on the PMMA is lifted with the resist as shown in Fig.3.8c. After the lift-off, only the gold, filling in the gap, remain.

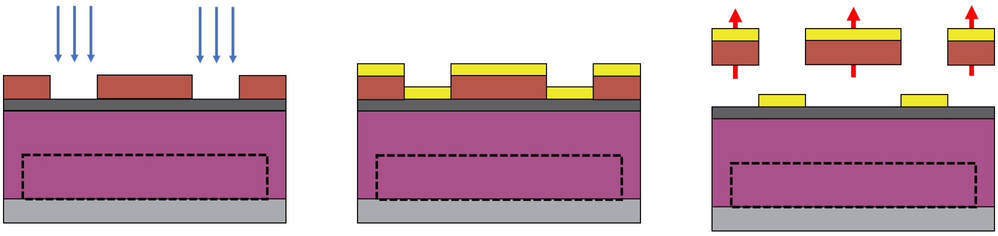

(A) (B) (C)

FIGURE 3.8: Lift-off step. (A) the E-beam step creates gaps in the resist. (B) 100 nm gold deposition by sputtering. (C) the resist is dissolved by acetone and the gold deposited on the resist is lift off during the process.

The acetone may not be sufficient to remove all the resist and the gold above (See 3.9). To improve the lift-off efficiency, the sample can be put in a sonication bath. The bath vibrates the sample with ultrasound waves, helping to take off the resist and the undesired gold. However, the sonication can sometimes damage the golden antennas, especially when the width is small. The scanning electronic microscopy pictures take after the processing show that the antennas with a width of $1\mu m$ are not affected by the sonication. However, the $250nm$ width antennas can occasionally be destroyed, as shown in Fig.3.10. For this reason, sonication has to be used as a last resort.

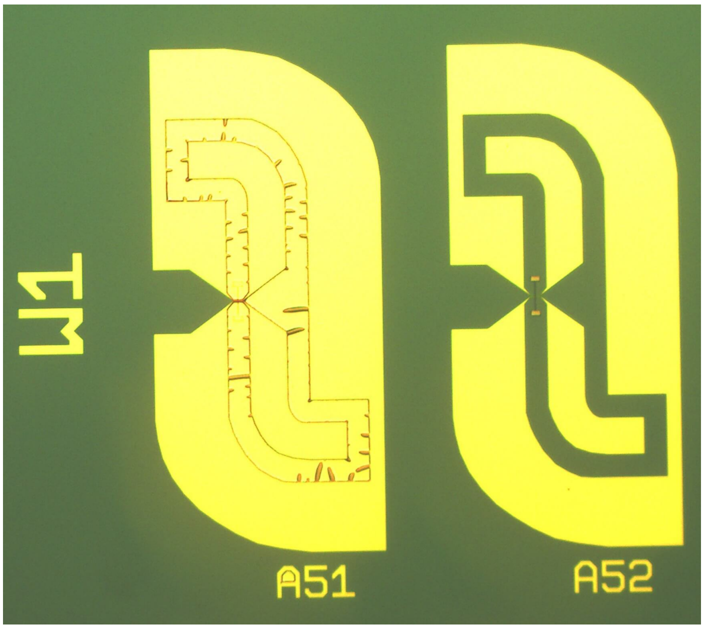

FIGURE 3.9: Microscope picture of two devices. On the right the lift-off was efficient, on the left, the lift-off failed to remove the gold between the electrodes.

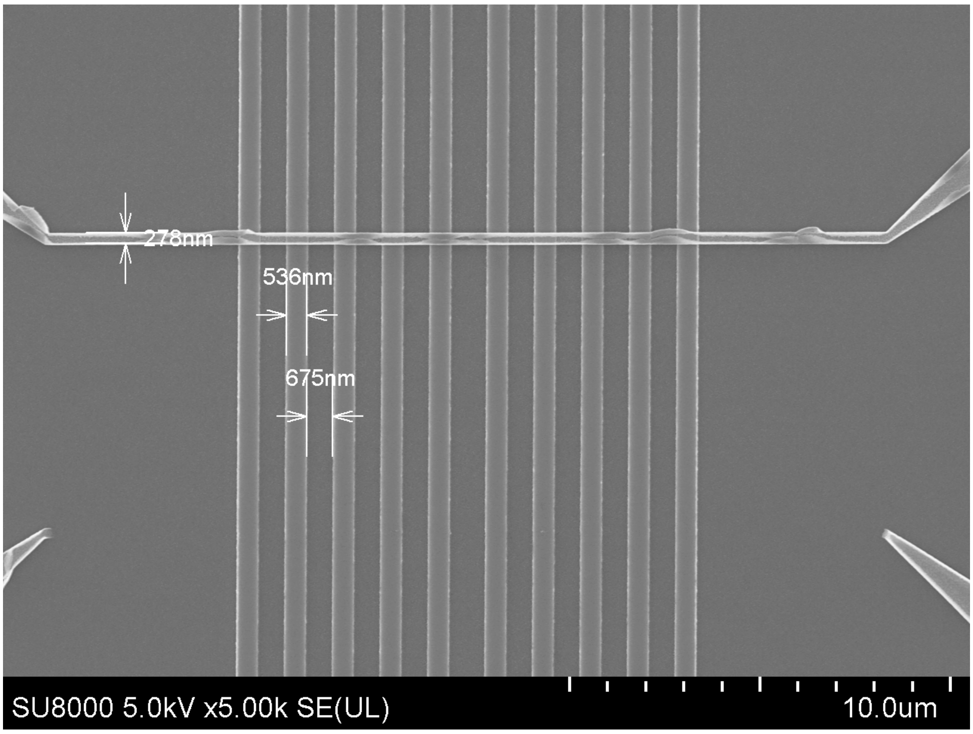

FIGURE 3.10: SEM picture after a sonication bath, the 250 *nm* antenna can be occasionally destroyed after the bath

3.3 STNO devices process flow

The second generation of devices, the STNO devices, has a process flow similar to the one develop in the previous section. However, there are several differences. Two lithographic step more a required, one for the definition of the pillar and one to open a gap inside the oxide layer to connect the electrodes. Furthermore, due to the additional complexity of the process, neither a hard mask for the etching of the waveguide and the pillar nor than a layer of SoC to planarize the surface is used. The steps of the process flow are illustrated in Fig.3.11.

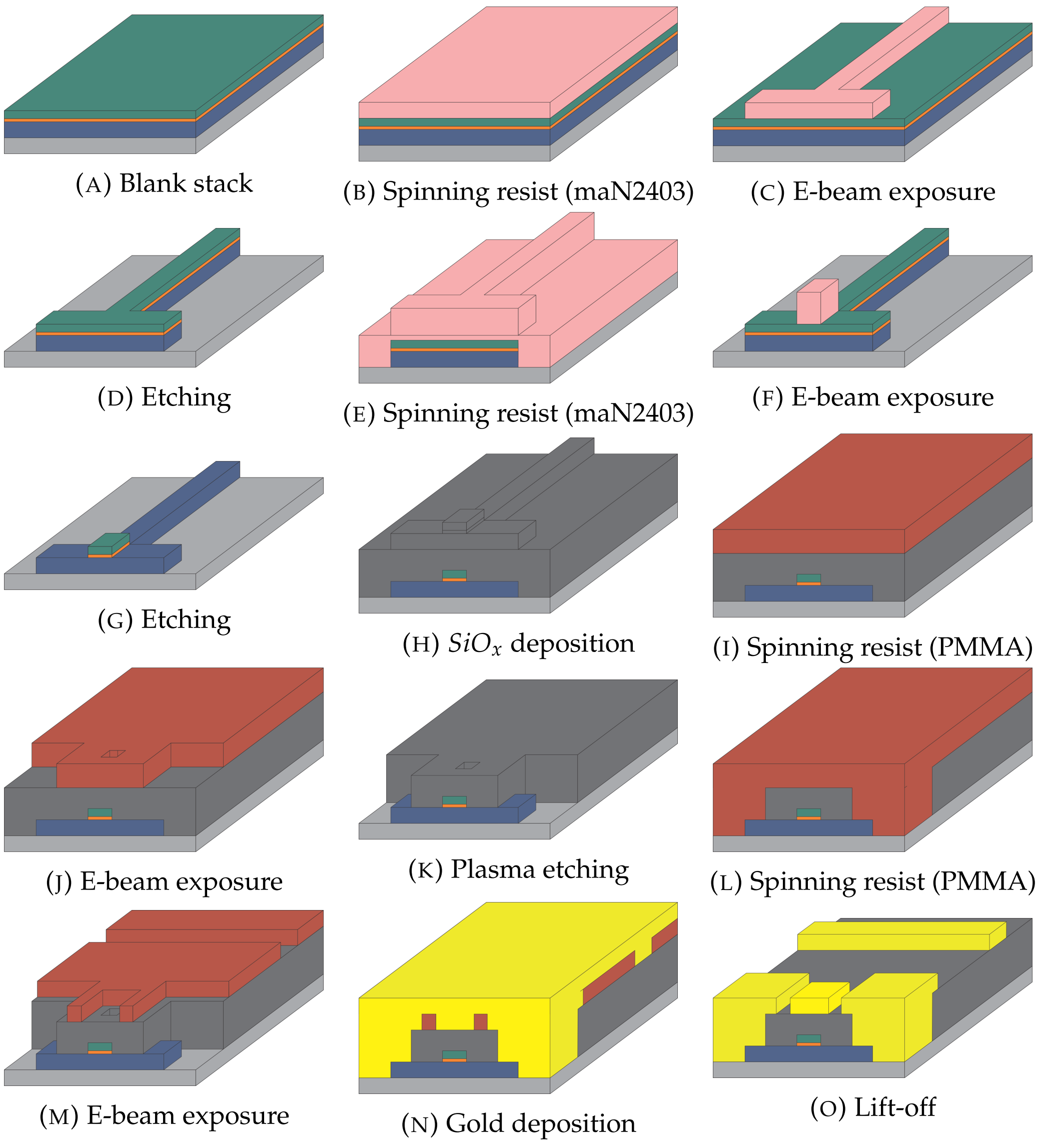

(A) Blank stack
(B) Spinning resist (maN2403)
(C) E-beam exposure
(D) Etching
(E) Spinning resist (maN2403)
(F) E-beam exposure
(G) Etching
(H) SiO_x deposition
(I) Spinning resist (PMMA)
(J) E-beam exposure
(K) Plasma etching
(L) Spinning resist (PMMA)
(M) E-beam exposure
(N) Gold deposition
(O) Lift-off

FIGURE 3.11: STNO devices process flow. Starting from the magnetic stack (A), a negative resist of maN2403 is spun (200 *nm*) (B) and after an E-beam exposure (C) the waveguide is etched (D). In the same way, a resist of maN2403 is spun (200 *nm*) (E), after a second E-beam exposure (F) the pillar is etched (G). A 60 *nm* layer of SiO_x is deposited (H). After the spinning of PMMA resist (I), a third E-beam exposure is performed (J) to open the contact in the SiO_x by plasma etching (K). The spinning of another PMMA resist (L), is used for a final E-beam exposure (M). A 10/100 *nm* layer of Ti/Au is sputtered (N) for the lift-off step of the antennas and the electrodes (L)

3.3.1 Magnetic waveguide and pillar definition

The waveguide is defined in a similar way that the antenna devices but without the use of a hard mask. Here, a kind of T-shape is patterned, the most extended stripe will be the waveguide itself, the pillar will be patterned at the center of the shape, and the two side area will be used to connect the bottom electrode to the free layer (see Fig.3.12).

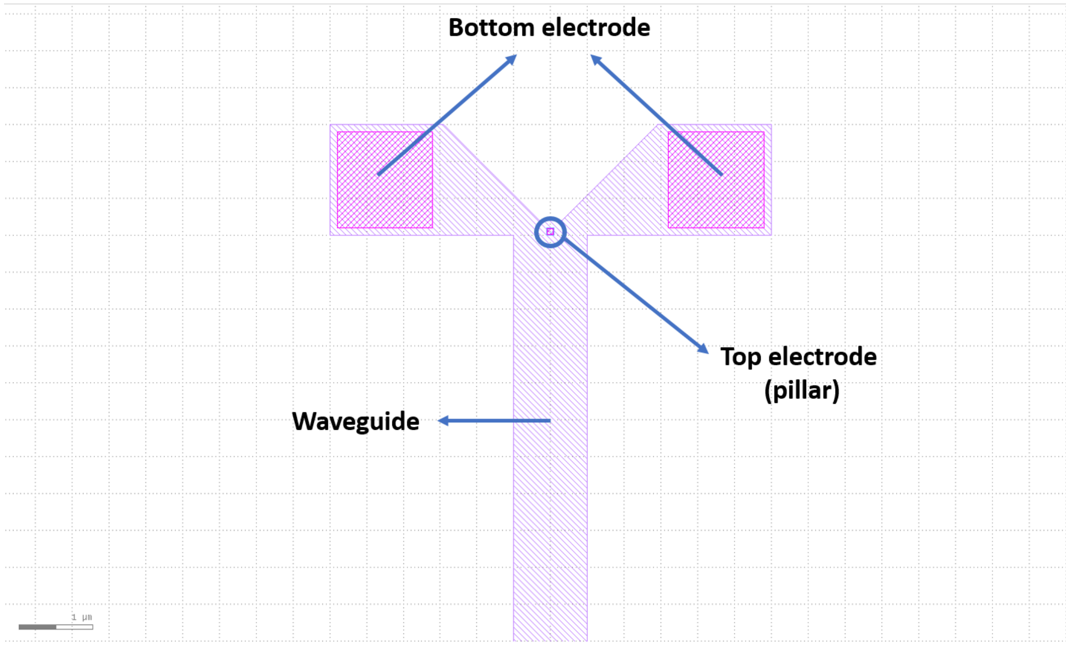

FIGURE 3.12: Design of the waveguides for the STNO device. During the first etching step, a T-shape is defined. The most extended stripe is the waveguides itself, and the side parts are used to connect the bottom electrodes.

The same negative resist used in the first process, 200nm thick, is spun. After an electronic lithography step and the development of the resist, the protective layer of maN2403 is patterned in the desired shape. The full stack is etched until the $Si0_x$ layers by ion milling (see Fig. 3.11b-d). The same step is repeated once again to define the pillar. After the spinning of the same resist, a second lithography step is performed to create a protective layer above the pillar area. The pillar is etched with a shorter time in order to stop the etching in the MgO layer just before the free layer (see Fig. 3.11e-g).

During the etching, sidewalls can be formed due to a backsputtering of the etched elements. When the ions reach the surface, particles are ejected. Close to the structure protect by the resist, a part of the material is deposited on the side of the structure by sputtering (see Fig.3.13a). The backsputtering creates a thin layer on the wall of the structure, as illustrated in Fig.3.13b, this layer is a mixture of the material etch and the resist. Fig.3.13d shows a sidewall formed during the process of the antenna device; for these devices, the sidewall is less critical because the waveguide is insulated with the antenna by an oxide layer. For the STNO devices, since the wall is partially metallic, the layer formed creates a conductive path between the top and the bottom layer, potentially shorting the tunneling junction and decreasing the efficiency of the spin-transfer torque effect. Therefore, it is crucial to design the devices in a way that the pillar is not patterned at the edges of the waveguide to avoid this problem. In this case, a sidewall is still formed, but the surface of contact between the two layers drastically decreases, as shown in Fig.3.13c.

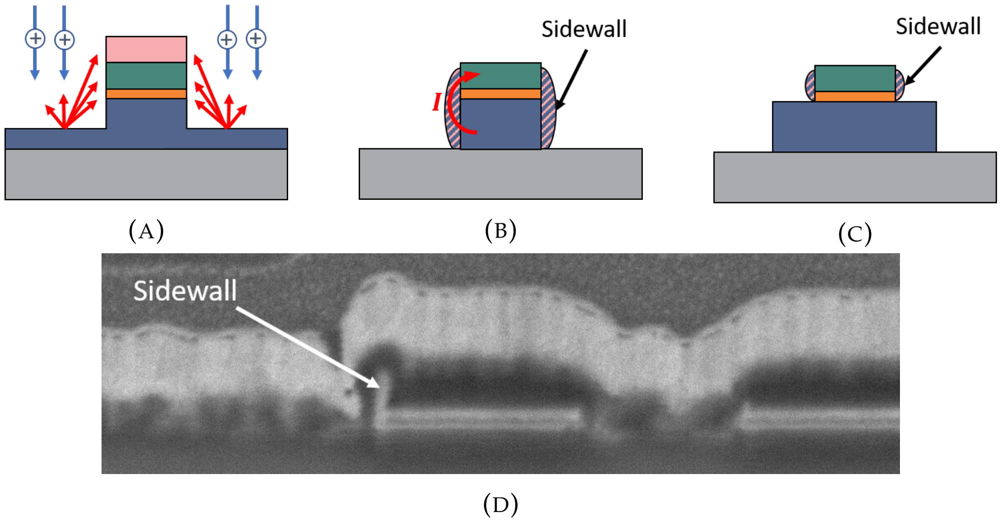

FIGURE 3.13: Backsputtering during the etching of the pillar. (A) The material etched is redeposited by sputtering effect on the sidewall of a closed structure. (B) The backsputtering creates a conductive layer shorting the MTJ. (C) To reduce this issue, the pillar is never patterned at the edges of the waveguides. (D) Example of a sidewall created during the fabrication of the antenna devices.

After the pillar and the waveguide etching, an insulator layer of SiO_x, 60 nm thick, is deposited on top of the structures. This layer has two roles, insulate the waveguide and the antenna used for the detection of the signal and prevent the shorting of the MTJ during the patterning of the top and bottom electrodes. As shown in Fig.3.14, without an oxide layer, the top electrode is in contact with both layers, and the current does not flow through the MTJ.

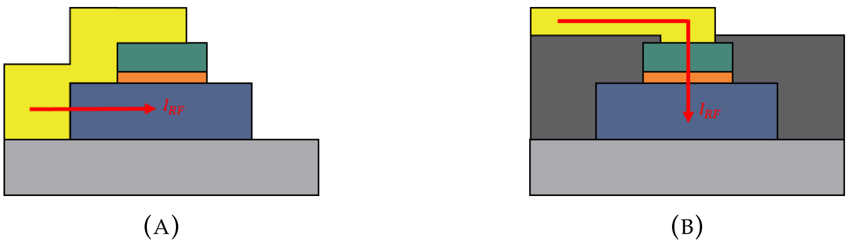

FIGURE 3.14: An insulating layer of SiO_x (in grey) is deposited to avoid a short circuit between the top and bottom electrodes during the patterning of the top electrode (in yellow).

3.3.2 Contact electrode and antenna pattering

To pattern the electrodes, two lithographic steps are required. A first exposure to open a gap through the oxide layer above the pillar to connect the top electrodes and above the lateral side of the waveguide to connect the bottom electrode, and a second one to deposit the antenna and the electrode. These steps are illustrated in Fig.3.11(i-o).

To open the contact area, a PMMA resist is spun on the top of the SiO_x layer. By an E-beam exposure, the gaps above the area of the contact electrode are opened by plasma etching. Nevertheless, when the electrodes are deposited, a residue of oxide can be present between the magnetic layers and the electrodes, reducing the quality of the contact by increasing the resistance at the interface. To ensure that all the SiO_x is removed in this area, the sample is over-etched during 1 minutes.

During the over-etching, the plasma could also etch the pillar and the free layer, degrading their proprieties. A test has been made to check the selectivity of the plasma on the SiO_x and the Ru capping layer on the top of the stack. The experiment shows that the free layer is not affected by the plasma. On the other hand, the pillar is etched by the plasma, as shown in Fig.3.15). However, the Ru layer (7 nm) is only etched after 2 minutes. Therefore the magnetic proprieties of the pillar will not be damaged by an over-etch of one minute. Furthermore, after 3 minutes of etching, the thickness of the stack doesn't decrease, indicating that when the Ru layer is fully etched, the first layer of platinum composing the SAF is not affected by the plasma.

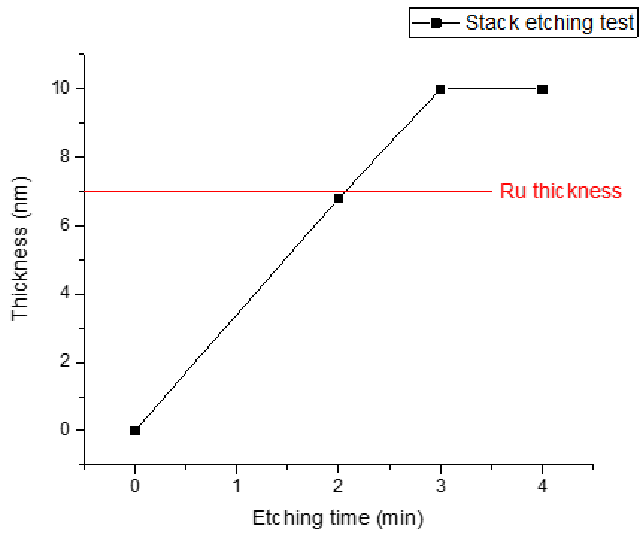

FIGURE 3.15: Etching time of the stack by a plasma. After an over-etch of 1 minute, the stack is 3.5 nm etched, which means that only the Ru capping layer of 7 nm is etched and that the magnetic stack is still protected after the over-etch.

The final step is the same as the previous process flow. The PMMA resist layer is exposed by lithography, creating gaps in the PMMA for the patterning of the antennas, perpendicularly to the waveguide, and for the electrode of the pillar above the gaps opened in the SiO_x in the previous step (see Fig.3.11. An adhesion layer made of titanium (10 nm) is deposited to ensure the good adhesion of a gold layer (100 nm) deposited just afterward without vacuum break. The PMMA is dissolved by acetone, removing with them the undesired gold by lift-off.

3.4 Process development

3.4.1 Lithography markers

When multiple lithographies exposures have to be performed, a point of reference is required on the mask to align each mask level correctly. For this purpose, e-beam markers are patterned on the sample corners. The e-beam tool is, therefore, able to deduce the position of every structure on the mask and processes each step with the correct relative position. Four markers in each corner have to be detected to correct the possible misalignment caused by the translation, rotation, magnification, and trapezoidal transformation; ensuring a high-grade precision. E-beam markers are composed of a cross and several squares of 5 μm, as shown in Fig.3.16.

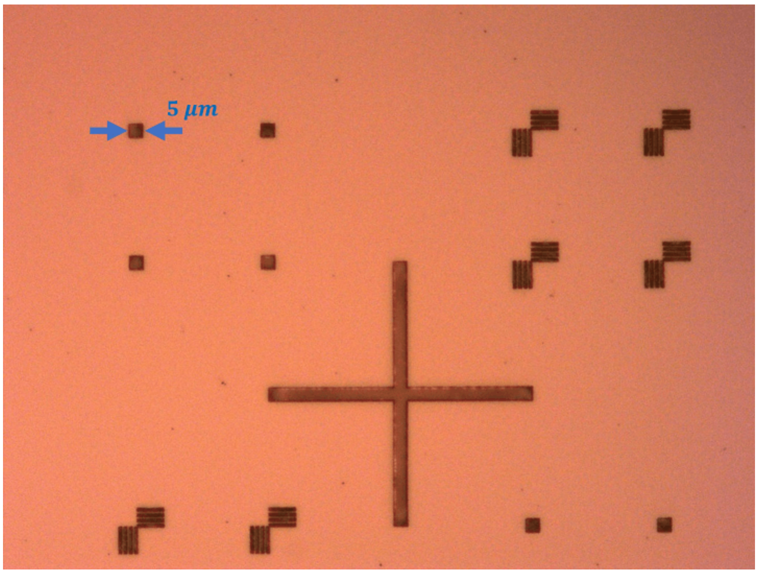

FIGURE 3.16: Microscopic picture of an E-beam marker acting as a reference position for mask level alignment. The marker is made of tantalum, 180 nm thick.

The detection is made by scanning the surface with the beam. When the electrons reach the markers, they are backscattered by the metal composing them. The measurement of the resultant signal is used to determine the relative position on the sample.

To enhance the backscattered signal and ensure the detection, the markers have to be made of metal with a high atomic number [36]. Usually, the markers are composed with gold ($Z_{Au} = 79$); however, some steps of the process had to be performed in a cleanroom with a lower level of contamination where gold isn't allowed. Other materials have been investigated to replaced gold. After several testing in the e-beam, the marker made of Tungsten ($Z_W = 74$) and tantalum ($Z_{Ta} = 73$), show the best contrast in the signal. To ensure the distinction, the markers have to be at least 100 nm thick and are usually processed with a thickness of 150-200 nm.

The markers are processed by e-beam lithography using PMMA resist. After the development, the metal is deposited on the resist with a thickness of 180 nm. A lift-off step in acetone remove the metal in the undesired area, and only the markers remain on the surface. Since the next steps of the process will etch the sample, the markers have to be protected to avoid their degradation. During the following e-beam exposures, beside the other structures, a protective layer has to be patterned on the area of the marker to protect them during the etching steps.

3.4.2 Dose test

To ensure the correct dimension of the structure patterned by electronic lithographies, dose tests have to be done with both resist used during the process. A dose test aims to determine the correct dose of the beam (i.e., the number of electrons injected by unit area in $\mu C/cm^2$). The dose range for these resists is somethings already develope. Nevertheless, the backscattered electrons depend on the material used and influence the dimension of the feature. For this reason, dose tests on the magnetic stack are performed.

maN2403

For the maN2403, the doses studied start from $200\mu C/cm^2$ to $550\mu C/cm^2$ with an increment of $25\mu C/cm^2$. The test is developed during two different times, 4 min, and 6 min. First, the shape realized in the resist after the development are inspected by SEM. After that, the sample is etched, the resist is removed, and the remaining structures are once again examined.

After the development, the thickness of the resist is measured with a profilometer for each dose. The measurements show that the structures for the doses below $325\mu C/cm^2$ have a lower thickness than the one expected for the resist, meaning that for these doses, the resist is underdeveloped. There is no point, therefore, to investigate these doses.

Three doses have been investigated in detail by SEM pictures. The doses inspected are: $375\mu C/cm^2$, $475\mu C/cm^2$ and $550\mu C/cm^2$. Tab.3.1 shows the width of the waveguide measured for each dose compared to the nominal one. The $375\mu C/cm^2$ with a development time of 4 minute shows the best result. The sample developed with 6 minutes was not investigated further due to a non-sharp profile in the resist. Indeed, even if the dimensions measured match, the dimensions on the surface are higher.

Nominal width	width measured					
	4′			6′		
	$375\frac{\mu C}{cm^2}$	$475\frac{\mu C}{cm^2}$	$550\frac{\mu C}{cm^2}$	$375\frac{\mu C}{cm^2}$	$475\frac{\mu C}{cm^2}$	$550\frac{\mu C}{cm^2}$
100	105	109	115	91.3	101	101
250	246	265	263	231	238	258
500	488	504	524	472	496	504
1000	984	1010	1050	954	1000	1020
5000	5000	5050	5200	4990	4990	5010

TABLE 3.1: maN2403 dose test. Dimensions of the structure patterned in the resist before etching the sample. Three doses are inspected by SEM for two development time (4 and 6 minutes).

The sample is etched and the resist removed. The same doses as before are inspected by SEM. It is expected that the dimensions are larger since the profile of the resist is never completely sharp and that the etching doesn't generate perfect vertical sidewalls. The structure size are shown in Tab.3.2, the dose returning the closest expected dimensions is the dose 375 μCcm^2. Nevertheless, since the dimensions are still larger, it has been decided to use a dose of 375 μCcm^2.

Nominal width	width measured		
	$375\frac{\mu C}{cm^2}$	$475\frac{\mu C}{cm^2}$	$550\frac{\mu C}{cm^2}$
100	121	138	-
250	311	297	300
500	559	560	583
1000	1030	1020	1040
5000	4730	4770	4755

TABLE 3.2: maN2403 dose test after etching the sample. The same three doses are inspected by SEM with 4 minutes of development.

PMMA

For PMMA, the doses studied start from $120\mu C/cm^2$ to $400\mu C/cm^2$ with an increment of $20\mu C/cm^2$. The profilometer shows that the doses lower than 220 $\mu C/cm^2$ have a thickness below 400 nm, meaning that the resist is not entirely removed and that the sample is underdeveloped. The dose higher than 320 $\mu C/cm^2$ shows profiles without sharp sidewalls, meaning that the sample is overdeveloped. Therefore, the dose of 240 $\mu C/cm^2$ and 300 $\mu C/cm^2$ are inspected by SEM. The 240 $\mu C/cm^2$ dose give a bad adhesion after the metal deposition, as shown in Fig.3.17. A part of the resist is still present below the electrodes degrading the adhesion, indicating that this dose is still underdeveloped. Consequently, the 300 $\mu C/cm^2$ dose is used during the process.

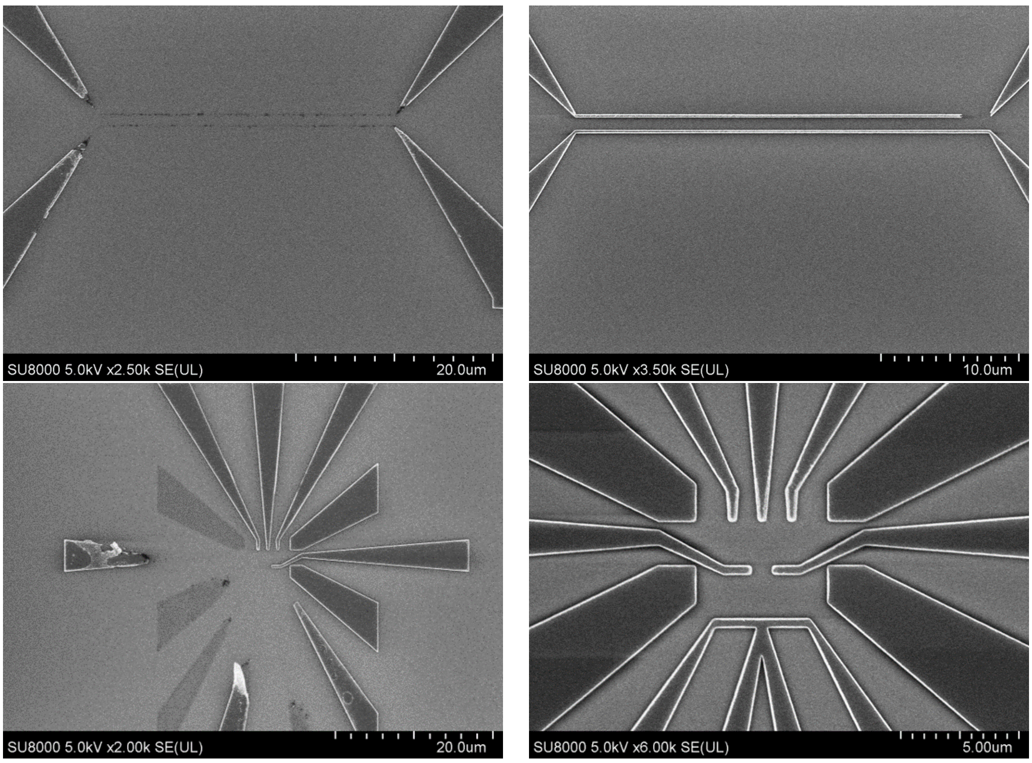

(A) 240 $\mu C/cm^2$ (B) 300 $\mu C/cm^2$

FIGURE 3.17: PMMA dose test. SEM picture after metal deposition. The 240 $\mu C/cm^2$ shows a poor adhesion.

3.4.3 Etching rate

It is required to know the etching rate of the material composing the stack to stop the etching at the right depth. For this purpose an etching test is performed, the sample is etching during different times, and a profilometer measures the depth. Tab.3.3 shows the pitch etched after a given time for the three wafers. From these measurements a mean etching rate of the full stack, including the substrate of SiO_x is computed:

$$ER_{mean} = 10.04\ nm/min. \tag{3.8}$$

	Depth measured (nm)			
	210 sec	240 sec	270 sec	300 sec
$d_{FL} = 10\ nm$	-	-	45.7	47.5
$d_{FL} = 5\ nm$	-	40	49	
$d_{FL} = 2.5\ nm$	37	40	-	-

TABLE 3.3: Etching test on the magnetic stacks with the different free layer thickness d_{FL}. The depth etched is measured for different etching time.

Technically, since the stack is composed of seven different material, a high number of point is required to perform the test. However, it is not needful to know the etch rate of every material on the top of the free layer since these materials are always etching together. Therefore, a mean etching rate (ER_{PL} in nm/min) is determined for the capping layer, the SAF, the reference layer as well as the MgO layer with a total thickness of $d_{PL} = 21\ nm$. The relation between the etching time (ET) used in the experiment and the etching rate of the free layer (ER_{FL}), the substrate (ER_{SiO_x}) and ER_{PL} is the following:

$$ET = \frac{d_{PL}}{ER_{PL}} + \frac{d_{FL}}{ER_{FL}} + \frac{d_{SiO_X}}{ER_{SiO_x}}. \tag{3.9}$$

$d_{PL} = 21\ nm$ is constant and d_{FL} depend on the stack; the thickness etch in the substrate d_{SiO_x} correspond to the depth measured minus $d_{PL} + d_{FL}$. From these equation, the three unknown etching rate are compute my the method of least squares.

Etching rate (nm/min)		
ER_{PL}	ER_{FL}	ER_{SiO_X}
8.85	7.72	14.58

TABLE 3.4: Etching rate of the perpendicular layers ER_{PL} including the capping layer, the SAF, the reference layer and the MgO junction; of the free layer ER_{FL} and of the $Si0_x$

.

Another way to estimate the etching rate of the perpendiculars layers is done by taking advantage of the magnetic properties of the stack. As shown in the previous section, the perpendicular layers have a spontaneous magnetization out-of-plane and the free layer in-plane. Blank samples are etched with different times and measured by VSM (see Fig.3.18) when the signature of the out-of-plane component is removed after, all the perpendicular layers are removed. From these experiments it takes between 105 and 120 sec to etch the out-of-plane layers, corresponding to an etching rate: $ER_{PL} \approx 11\ nm$. Compared to the previous etching rate computed before (see Tab.3.4), it is slightly above. Notice also that the etching rate of the $Si0_x$ show in this table is higher than the rate expected with the ion miller used for the etching. These difference come from the variability of the etching process and the precision of the profilometer.

For the etching of the full stack during the process, the mean value is used to stop the etching. Since the stack is overetched one minute to asses the complete etching of the waveguide, a precise of the etching stop is not critical for this step. For the pillar definition where the etching has to stop above the free layer is appeared that it is difficult to stop the etching reliably. For this reason, it has been decided to use another etching instrument in the semi-industrial cleanroom of IMEC. The tool can measure the magnetic properties of the sample during the etching. Therefore, the etching stops not after a given time, but when the magnetic properties correspond to the properties of the free layer only.

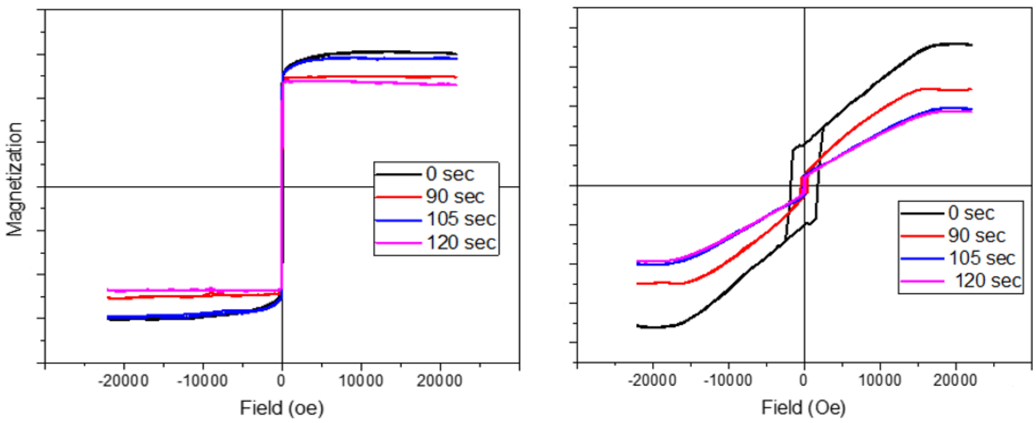

(A) In-plane measurement (B) Out-of-plane measurement

FIGURE 3.18: Etching test by VSM. The samples are etched at different times, and the magnetic proprieties are measured. After 120 sec, the behavior of the magnetic layers with a polarization out-of-plane disappear, indicating that these layers are fully etched.

3.5 Conclusion

In this chapter, the proprieties of the MTJ stack have been investigated. The SAF and the reference layer show the behavior of a hard magnet, suitable for the polarization of spin current and the free layer has the proprieties of a soft magnet proper for spin wave excitation. The spontaneous polarization of the perpendiculars layers allows the injection of a spin current with magnetic moment perpendicularly to the magnetization of the free layer.

The process of fabrication for both STNO device and antenna devices have been present as well as the development required to achieved the fabrication of the devices. During the time of this thesis, only the antenna devices have been completely processed, the fabrication of the STNO is actually ongoing.

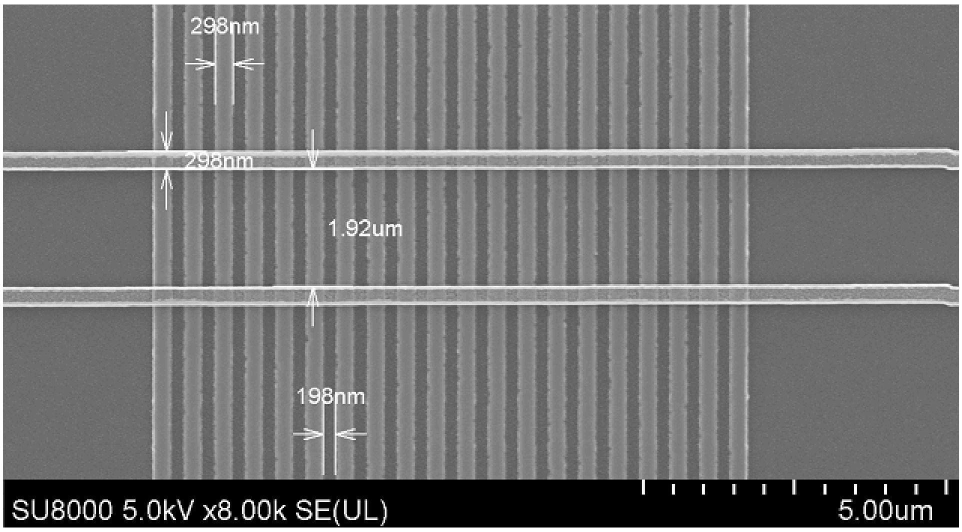

FIGURE 3.19: SEM of an antenna device. The dimensions of the waveguide and the antenna are higher than the nominal value (250 *nm*).

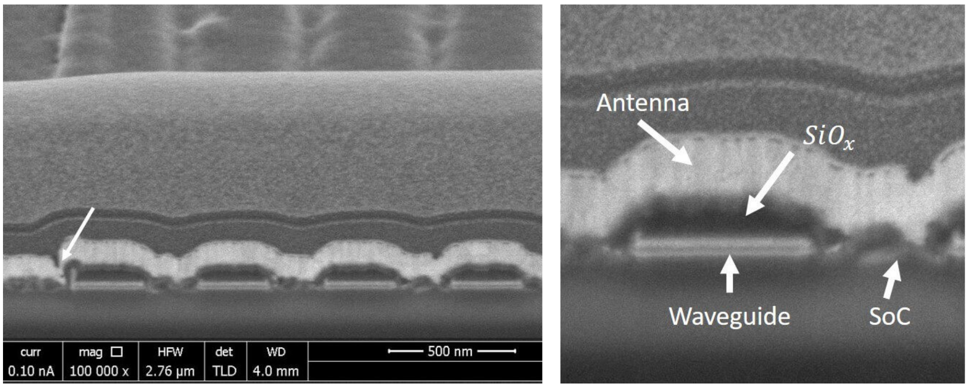

FIGURE 3.20: Cross-section of an antenna device. The antenna is not flat due to a too deep recession.

The inspection of the antenna devices returns that the fabrication has been done correctly. In most of the devices, the waveguides and the antenna are correctly defined, even though the dimension are generally higher than expected for the antennas as well as the waveguides as shown in Fig. , indicating that the dose determined during the dose test is too high.

The cross-section of the devices is shown in Fig.3.20. The waveguides are well defined, yet the antenna above present a bump profile. The picture shows that no SoC remains between the waveguides and the antenna, only between the waveguides but with a thickness lower than the SiO_x layer. It means that the recession etches too deeply the SoC; therefore, the surface after the planarization is not perfectly flat. As explained before, the irregularity in the profile during the deposition of the antenna can lead to a decrease of the thickness in some area, as shown on the left picture, and can potentially create an open circuit even tough in this case the lower thickness is mostly due to the formation of a sidewall.

Nevertheless, the electrical measurements detail in the next chapter show that less than 5 % of the devices have short circuits between the antennas, meaning that they are insulated with the waveguides, or have broken antenna.

Chapter 4

Electrical characterizations

In this section, the electrical properties of the devices will be measured via microwave technique and analyzed. Since the antenna devices were processed during this thesis, the measurements are performed for these devices only. The spin waves are characterized in MSSW mode, where the external field is perpendicular to the waveguide (see section 1.4.1). To understand the propagation of the spin wave in the free layer, the different available parameter of the devices are varied.

The goal is to describe the propagation in the free layer but also to understand the influence of the other layers on the spin wave as well as the possible detection of others modes inside the SAF and the reference layers.

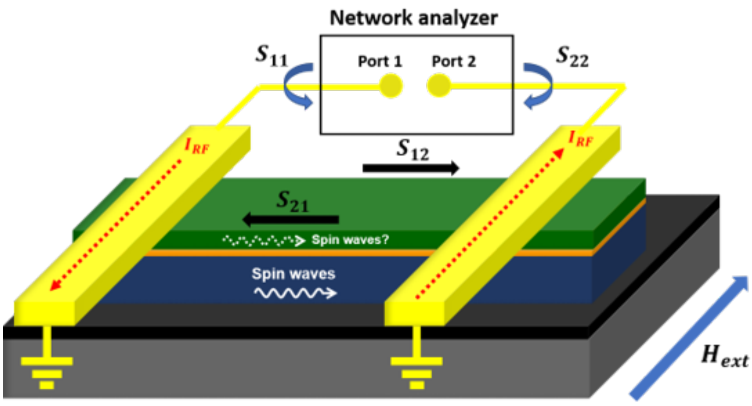

FIGURE 4.1: Spin waves antenna devices measured. The measurements are done by a vector network analyzer. The antenna connected to the port 1 emits spin waves and the antenna connected to the port 2 detected the spin wave signal. The VNA return the scattering parameters.

4.1 Measurement setup

The characterization is performed using radiofrequency measurements. The installation used is composed of two microprobes between an electromagnet. The probes inject and detect the RF current inside the device for a broad range of frequencies. The signal is analyzed by a vector network analyzer (VNA). The electromagnet is used to tune the external field inside the devices. A microscope on the top of the setup is used to connect the microprobes to the electrodes of the devices (see Fig.4.2).

The VNA is used to characterize the behavior of an electrical network as a function of the input signal. For a network of N port, a VNA return a $N \times N$ matrix of parameters called the scattering parameters (S-parameters) at each frequency. For the present studies, each antenna are connected to a port ($N = 2$).

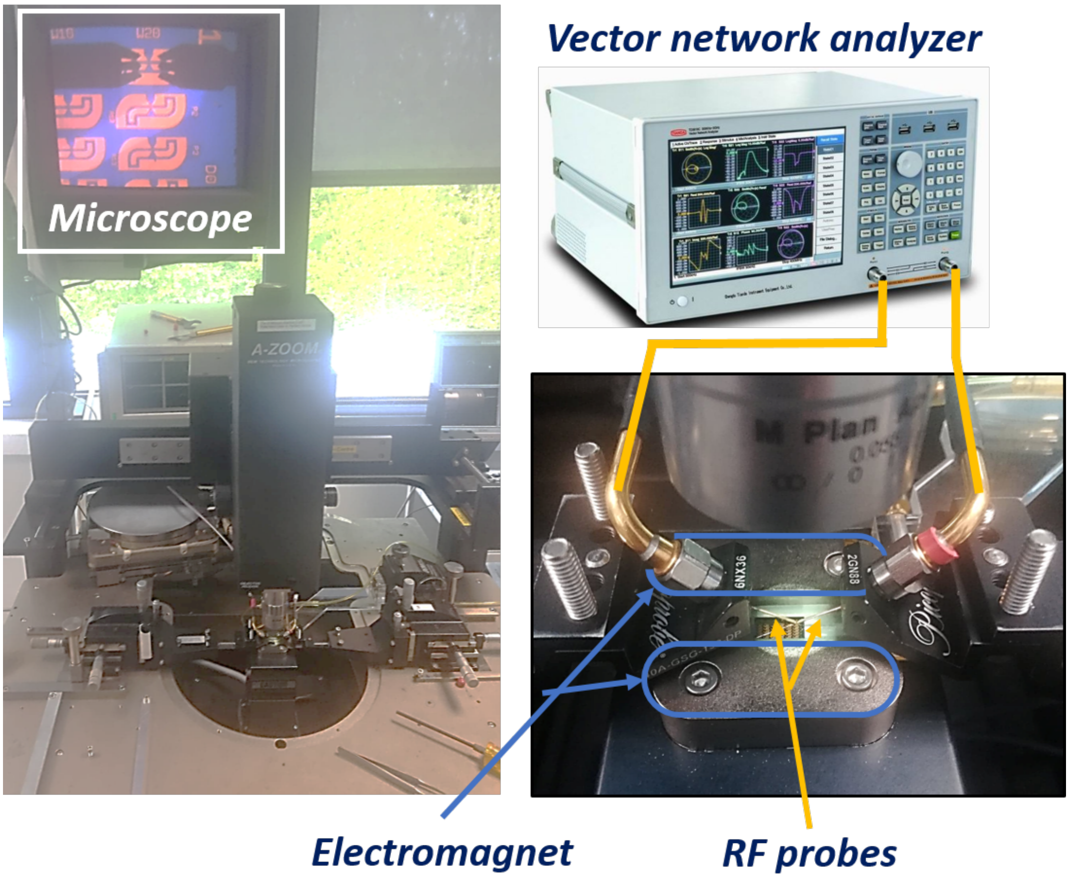

FIGURE 4.2: RF setup for spin waves characterization. Two micro-probes connected to the device are placed between an electromagnet. The magnetic field inside the device can be modified. The signal is analyzed by a vector network analyzer.

The S_{ij} parameter is a complex unitless number and link the incident power wave a_j on the port j and the reflected power wave b_j on the port i. For a two-port network:

$$\begin{pmatrix} b_1 \\ b_2 \end{pmatrix} = \begin{pmatrix} S_{11} & S_{12} \\ S_{21} & S_{22} \end{pmatrix} \begin{pmatrix} a_1 \\ a_2 \end{pmatrix}. \quad (4.1)$$

a_i and b_j are normalized tensions and can be expressed by the tension and the intensity current measured in the port i. Assuming that the inputs of the network system have the same reference impedance Z_0 (usually 50Ω), the incident power wave a_i and the reflected power wave b_i can be defined as [37]:

$$a_i = \frac{V_i + Z_0 I_i}{2\sqrt{Z_0}} \quad \text{and} \quad b_i = \frac{V_i - Z_0 I_i}{2\sqrt{Z_0}}. \quad (4.2)$$

Considering an incident power wave at port 1 (a_1), a part is reflected in port 1 (b_1), and another is transmitted toward the port 2 (b_2). If the network is loaded with the same reference impedance Z_0, no power coming from the port 2 is reflected in the system and $a_2 = 0$. In this case, S_{11} describe the ratio between the power reflected and emitted at the port 1 and S_{21} the ratio between the power transmitted at the port 2 compared to the power emitted from the port 1.

4.2 Signal at zero field

Fig4.3 shows the scattering parameters S_{11} and S_{21} at zero field. Since the antennas are not connected to each other, most of the power is reflected (S_{11} is high) and only a few fraction is transmitted (S_{21} is low) at low frequency. When the frequency increases, the power transmitted increases, this effect can be due to rather an inductive effect between the two antennas or capacitive effect.

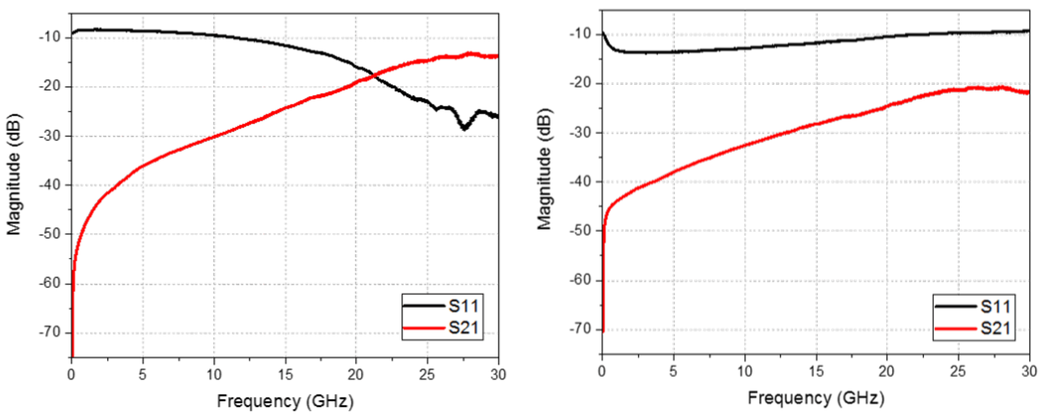

(A) Antenna width: 1 μm (B) Antenna width: 250 mm

FIGURE 4.3: Scattering parameters S_{11} and S_{21} without an external field on a device with $d = 10\ nm$, $P = 2\ \mu\ m$, $W = 20\ \mu m$ and for to different antenna with. The antennas are an open circuit, at a low frequency most of the power reflected. At higher frequency, the transmission between port 1 and 2 increase due to inductive and capacitive effects.

From the relations (4.1) and (4.2) it is possible to represent the impedance parameters Z_{ij} of the two port system with the following circuit:

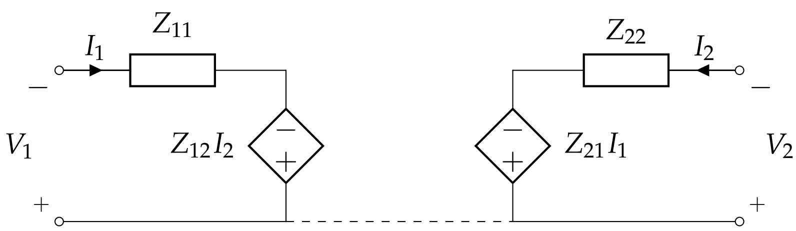

The impedance parameters link the current and the voltage by the relation:

$$\begin{pmatrix} V_1 \\ V_2 \end{pmatrix} = \begin{pmatrix} Z_{11} & Z_{12} \\ Z_{21} & Z_{22} \end{pmatrix} \begin{pmatrix} I_1 \\ I_2 \end{pmatrix}. \tag{4.3}$$

Z_{11} correspond to the impedance of the line (the antenna and the electrodes) connected to port 1 if no power are transmitted ($Z_{12} = 0$ and can be expressed as:

$$Z = R + jX, \tag{4.4}$$

where R and X are respectively the resistance and the reactance. The reactance describes the contribution of the inductive X_L and capacitive effects X_C:

$$X = X_L + X_C = \omega L - \frac{1}{\omega C} \quad , \tag{4.5}$$

where ω is the frequency of the signal. When X is positive, the inductive effect is dominant, when X is negative, the capacitive is predominant. To avoid a reflection of the signal coming from the VNA and the antenna; and isolated a signal coming from the spin wave only, the impedance Z_{ii} has to match the impedance of the VNA equal to $Z_0 = 50\Omega$, meaning a resistance $R_{ii} = 50\Omega$ and a reactance $X_{ii} = 0$.

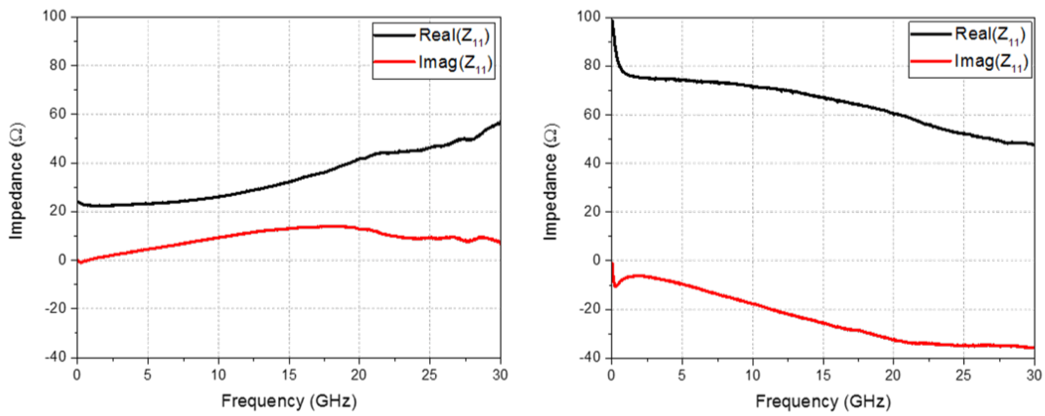

(A) Antenna width: 1 μm (B) Antenna width: 250 mm

FIGURE 4.4: Real and imaginary part of the $Z-$parameters Z_{11} and S_21 without an external field on a device with $d = 10\ nm$, $P = 2\ \mu m$, $W = 20\ \mu m$ and for to different antenna with. The real part describes the resistance R of the antenna and the imaginary part the reactance X. The 1 mum antenna shows a dominent inductive effect ($X > 0$) and the 250 nm antenna shows a capactif effect ($X < 0$).

Fig.4.4 shows the impedance Z_{11} of the devices with $1\mu m$ and $250nm$ antenna width. The devices never fully match the reference impedance of 50 Ω. The resistance is lower at low frequency for the devices with the larger antenna compared to the resistance of the smaller devices. This result is explained by the fact that the resistance increases when the size of an electrical conductor decreases. For the $1\mu m$ antenna, the inductive effect is dominant indicating that the increase of the power transmitted (i.e., increase of S_{21}) with the frequency is caused by an inductive effect. The $250nm$ antenna shows a capacitive effect, because the antennas gets a resistance larger than the Si substrate. This capacitive coupling creates a movement of charges in the substrate, causing a loss of power in the Si.

4.3 Spin wave signal

The behavior of scattering parameters shown in the previous section depend only on the electrical electrodes and antennas of the devices. Nevertheless, it is possible to extract the signal originating from the spin wave at a given external magnetic field, by subtracting the signal zero field. Assuming that the other properties are independent from the external field, the effect of the devices electrical part doesn't evolve with the magnetic field. Moreover, at zero field the waveguides aren't saturated, magnetic domains are present and their domain walls block the spin wave propagation. The signal measured a zero field is therefore used as a reference to extract the spin wave component of the signal:

$$S_{ij}^{SW}(H_0) = S_{ij}(H_0) - S_{ij}(0). \tag{4.6}$$

The parameter of interest here is S_{21}^{SW} (or S_{12}^{SW}) since it is the ratio between the power generated by the spin wave in the antenna connected to the port 1 and the power consumed by the other antenna to emit this spin wave (and inversely for S_{12}^{SW}). These parameters depend mostly on the current generated by the oscillation of the magnetic flux induced by the spin wave below the antenna. By the Faraday's law, this current depends on the variation of the magnetic flux:

$$I \propto \frac{d\boldsymbol{M}(t)}{dt}. \tag{4.7}$$

From the spin wave equation (1.27) extracted in section 1.4 and by adding a exponential decay term $\beta\boldsymbol{k} \cdot \boldsymbol{r}$ where β is a mode-dependent function of the Gilbert damping, it can be shown that the S-parameter depends on the phase and the amplitude of the wave [38]:

$$S_{12}^{SW} \propto me^{-i\boldsymbol{k}\cdot\boldsymbol{r}-\beta\boldsymbol{k}\cdot\boldsymbol{r}}. \tag{4.8}$$

The S_{21}^{SW} measured for one devices is plotted in Fig.4.5a, the real and imaginary part as well as the modulus are displayed. The curve shown is a typical representation of spin waves. A non-zero signal is detected in a finite frequency band. The range of frequency is determined by the maximum number of k-vectors that can be excited by an antenna. Starting from $k = 0$ (corresponding to the ferromagnetic resonance f_{FMR}) to a cut-off k-vector corresponding to the minimum wavelength that can be excited. Indeed an inductive antenna cannot emit a spin wave with a wavelength smaller than its width. The maximum k-vector is, therefore around:

$$k_{max} = \frac{2\pi}{A}, \tag{4.9}$$

where A is the width of the antenna. From the dispersion relation (1.38) of the MSSW mode explained in section 1.4.1 it is possible to link the range of k-vector with the frequency band: $[f_{FMR}, f(\boldsymbol{k}_{max})]$ as shown in Fig.4.5b.

The modulus of S_{12} describes the amplitude of the wave (i.e., the angle between the magnetization and the external field). The wave is maximum after the FMR and decreases with the frequency (decrease with $\boldsymbol{k}$). From the equation 4.8), the real and imaginary part can be expressed as:

$$Re(S_{12}) \propto me^{-\beta\boldsymbol{k}\cdot\boldsymbol{r}}cos(\boldsymbol{k}\cdot\boldsymbol{r}), \tag{4.10}$$

$$Im(S_{12}) \propto me^{-\beta\boldsymbol{k}\cdot\boldsymbol{r}}sin(\boldsymbol{k}\cdot\boldsymbol{r}). \tag{4.11}$$

The real and imaginary part gives information about the phase $\boldsymbol{k} \cdot \boldsymbol{r}$ and the amplitude $e^{-\beta \boldsymbol{k} \cdot \boldsymbol{r}}$ of the signal, both with a phase shift of $\frac{\pi}{2}$.

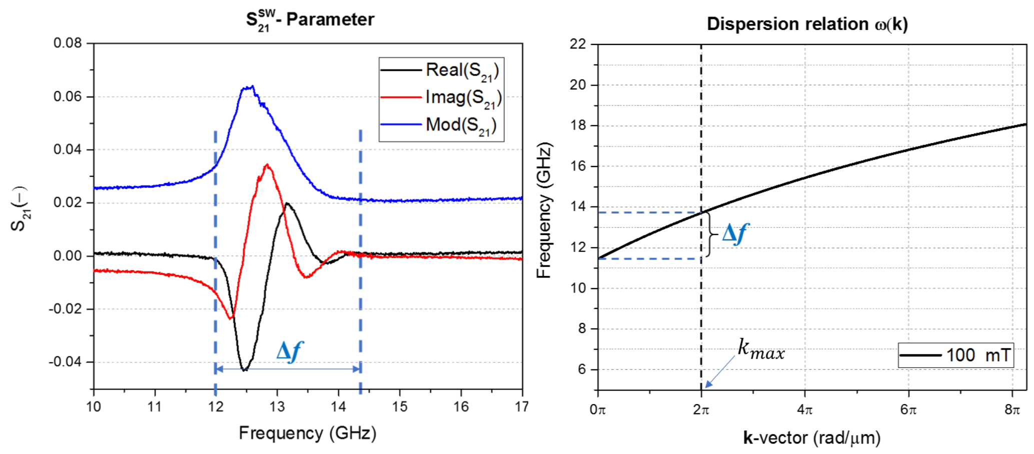

(A) S_{21}^{SW}-Parameter (B) Dispersion relation $f(\boldsymbol{k})$

FIGURE 4.5: (A) The real, imaginary part and the modulus of the signal measured after subtraction at zero field for a device with a FL layer thickness $d = 10\ nm$, an antenna width $A = 1$, a waveguide width $W = 5\ \mu m$ and propagation distance $P = 1\ \mu m$ in external field $H_0 = 100\ mT$. The modulus is offset with a 0.02 positive value. (B) Dispersion relation of the MSSW mode computed from the analytical relation (1.38), with $d = 10\ nm$, $H_0 = 100\ mT$ and a magnetic saturation $M_S = 1250\ emu/cm^3$. The dash line correspond to the maximum k-vector for $A = 1\ \mu m$.

Finally, the comparisons between S_{12} and S_{21} in Fig.4.6 shows the asymmetric behavior of the MSSW mode. The non-reciprocity in such thin films is due to the chirality of the field generated by the antennas.

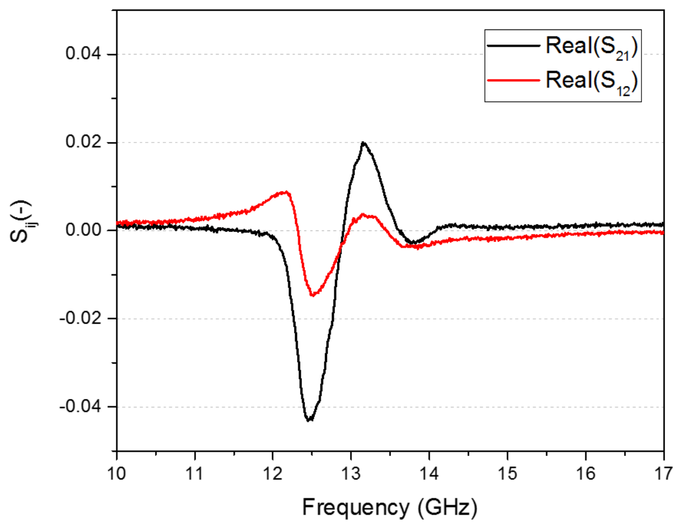

FIGURE 4.6: Comparison between the parameter S_{21} and S_{12}. The difference of efficiency show the asymmetric behavior of the MSSW mode.

For these reasons, the real part of S_{21} will the main parameter of intrest, in the next section, since it gave information about the phase and the amplitude, and show a higher signal amplitude. To study the wave propagation, the influence of each parameter will be analyzed by keeping the other constant. The parameters of interest are the applied magnetic field H_0, the propagation distance P, the width of the antenna A, the width of the waveguide W and the thickness of the free layer d.

4.3.1 influence of the field H_0

The dispersion relation derived in section 1.4.1 for the MSSW mode:

$$f(\boldsymbol{k}) = \gamma\mu_0\sqrt{H_0\left(H_0 + M_s\right) + \frac{M_s^2}{4}\left(1 - e^{-2kd}\right)}, \tag{4.12}$$

shows that the frequency increases with the magnetic field H_0 for the same k-vector. As shown in Fig.4.7b, the evolution of the dispersion relation with the magnetic field modifies the frequency band of the signal (Fig.4.7a), the band shifts in frequency when the field increases and the band width shrinks. The dispersion relations are computed with the equation (4.12) for a thickness $d = 10nm$ and a magnetic saturation $M_S = 1250emu/cm^3$, measured for the free layer in the previous experiment (see section 3.1.1). This relation gives an analytical approximation of the frequency band for a $1\mu m$ antenna:

- $[f_{FMR}, f_{max}]_{35mT} = [6.6, 10]\ GHz$,
- $[f_{FMR}, f_{max}]_{100mT} = [11.4, 13.7]\ GHz$,
- $[f_{FMR}, f_{max}]_{160mT} = [14.7, 16.5]\ GHz$.

Fig.4.7a shows the experimental signals measured on a device with a waveguide width of $5\mu m$, a $1\mu m$ antenna, and a free layer thickness of $10nm$. By comparing these curves with the analytical model, it is shown that the signal measured is consistent with propagating spin waves in the Damon-Eshbach mode inside a $10nm$ thick layers of CoFeB.

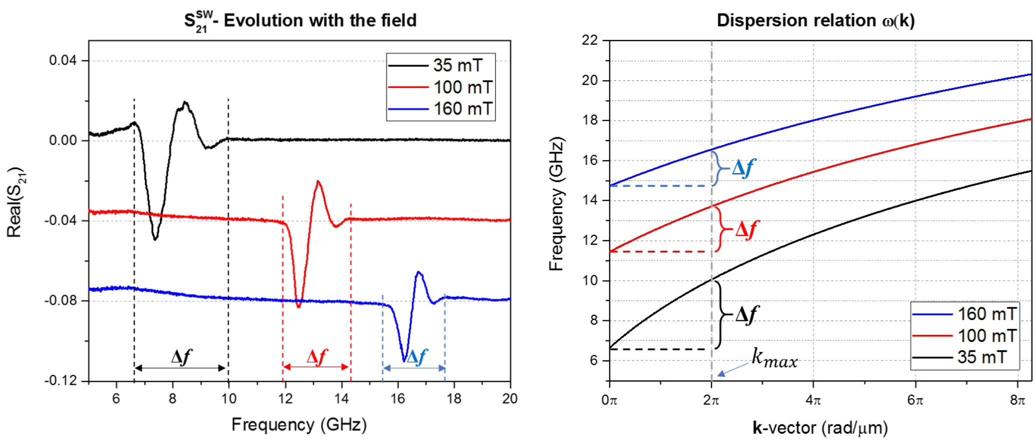

(A) S_{21} - Parameter (B) Dispersion relation $f(\boldsymbol{k})$

FIGURE 4.7: Evolution with the field H_0. (A) Signal at three different field measured on devices with $d = 10\ nm$, $A = 1$, $W = 5\ \mu m$ and $P = 1\ \mu m$, the curves are offset. (B) Dispersion relation of the MSSW mode computed from the analytical relation (4.12) at different field.

The analytical f_{FMR} and the f_{max} is close to the experimental measurement even though at high field the experimental f_{FMR} and f_{max} tend to be higher than the expectation, moreover, this difference is larger when the field increases. The origines of this deviation are detail at the end of this section (see section 4.4).

Furthermore, the equation (4.12) does not take into account neither the effect of finite waveguide width on the propagation nor the influence of the other magnetic layers. Nevertheless, the variation is sufficiently low to claim that the influence of the other layers on the evolution of the propagation with the field is small for the devices measured.

4.3.2 Propagation distance P

The same type of device as before, with $W = 5\ \mu m$, a $A = 1\ \mu m$, and $d = 10\ nm$ is measured as a function of the distance between the antennas P in Fig4.8a. Only one magnetic field of 100 mT is considered, and the three curves correspond to different propagation distance P (distance between the antenna).

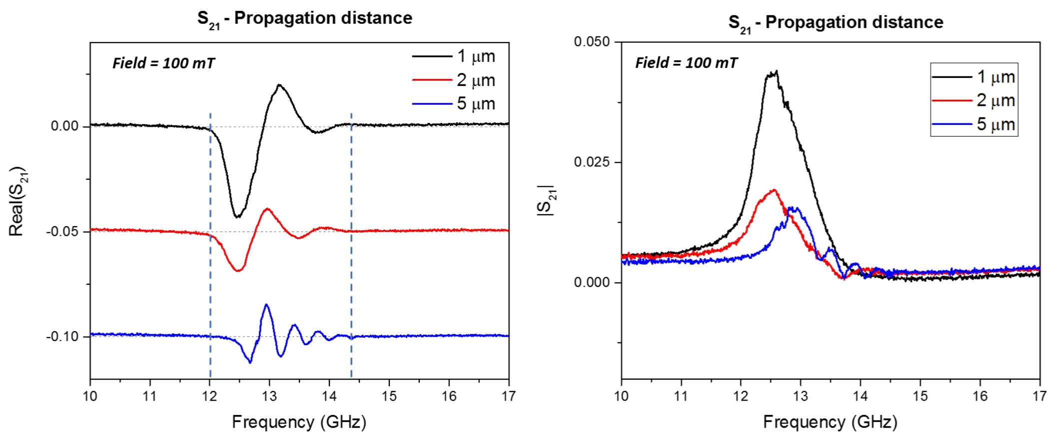

(A) Real(S_{21}) (B) $|S_{21}|$

FIGURE 4.8: Evolution with the propagation distance P. (A) Real part of the signal measured for three different P with $d = 10\ nm$, $A = 1$, $W = 5\ \mu m$ with $H_0 =\ mT$. The frequency band remain the same but the number of phase rotation increased, the curves are offset. (B) Modulus of the signal. The amplitude of the spin wave decrease exponentially with $\boldsymbol{r}$.

Since the dispersion relation depends only on the device waveguide dimensions and that k_{max} depend only on the size of the antenna, the frequency band remains the same when the propagation distance varies. Fig.4.8b shows that the signal amplitude decrease with the propagation distance $\boldsymbol{r}$ due to the term $e^{-\beta \boldsymbol{k}\cdot\boldsymbol{r}}$ in the equation (4.8). If the frequency band remains the same, the number of phase rotations, corresponding to the phase change of 2π in the wave, increases. It's explained by the term $e^{i\boldsymbol{k}\cdot\boldsymbol{r}}$ in the relation (4.8). For the same frequency band (i.e., the same k_{max}), the number of phase rotations n increases with $\boldsymbol{r}$:

$$\boldsymbol{k} \cdot \boldsymbol{r} = 2\pi n. \tag{4.13}$$

At the FMR (i.e., infinite wavelength), the phase detected is the same. When the frequency increases, the change of the detected phase evolved faster with the frequency when the propagation distance increases. This phenomena is illustrated in Fig.4.9 using a schematic.

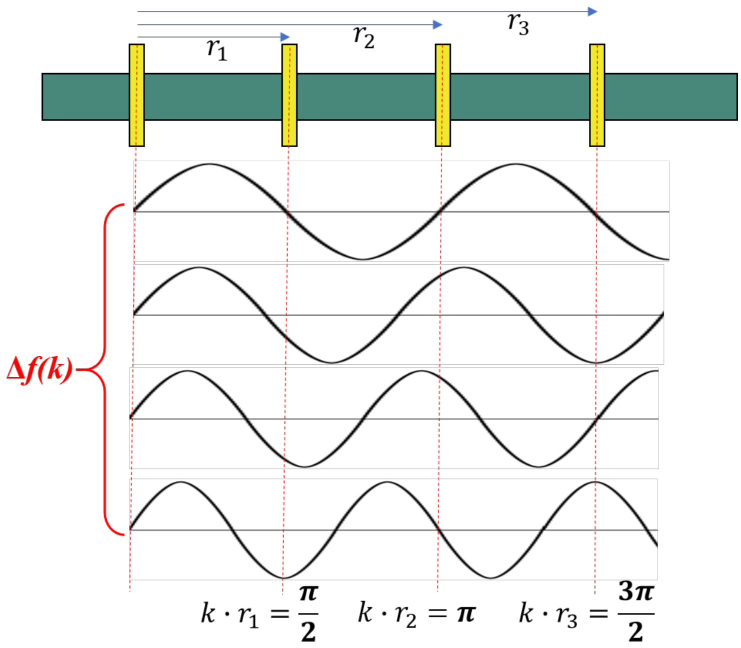

FIGURE 4.9: The antenna with a distance r_1 from the spin waves source detected a phase from 0, for the lower frequency, to $\frac{\pi}{2}$ for the highest frequency. For the distance r_2, a phase from 0 to π is detected, and for r_3, a phase from 0 to $\frac{3\pi}{2}$: For the same frequency band Δf, the changed of phase detected in this range increase with the distance of propagation.

4.3.3 Antenna width A

Once again, the same type of device with $W = 5\ \mu m$, $d = 10\ nm$ and $H_0 = 100\ mT$ is measured with $P = 1\ \mu m$ for different antenna widths A. In Fig.4.10a, the black curve is the signal detected and emitted with a 1 μm antenna and the red one the signal with a 250 nm antenna. The decrease of the antenna width increases the number of k-vectors emitted; from $2\pi\ (rad/\mu m)$ for $A = 1\ \mu m$ to $8\pi\ (rad/\mu m)$ for $A = 250 nm$ (see equation (4.9)). As shown in Fig.4.10b, the scaling down of the antenna increases the frequency band.

The number of phase rotation $\frac{k \cdot r}{2\pi}$ also increases, in this case, it is caused by the increase of the k-vector, however, for the same range of frequency the number of phase rotation is equal for the two different antennas since the propagation distance is the same, meaning that at a given frequency, the phase detected is the same. The curve shows that it is the case close to the FMR, at a higher frequency, a phase shift is observed between the curve. The reason is that the propagation distance is slightly higher for the larger antenna; in reality, the effective distance is more close to the distance between the centers of the antennas than the gap (here 1 μm). For the 1 μm antenna, the effective distance $\boldsymbol{r_{A=1}} \approx 2\ \mu m$ and for the 250 nm antenna, the effective distance $\boldsymbol{r_{A=0.25}} \approx 1.5\ \mu m$. It is consistent with the fact that between 12 and 14 GHz, the phase rotation is approximately 2π for $A = 1$ and $\frac{3\pi}{2}$ for $A = 0.25$.

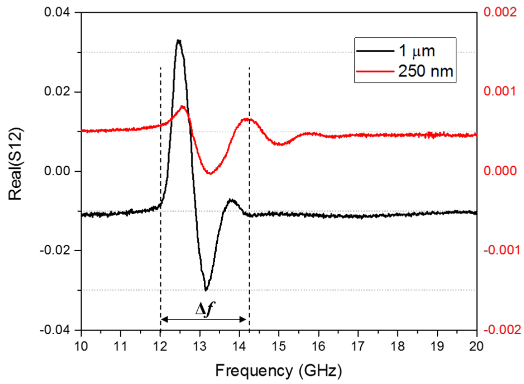

(A) S_{21} - Parameter

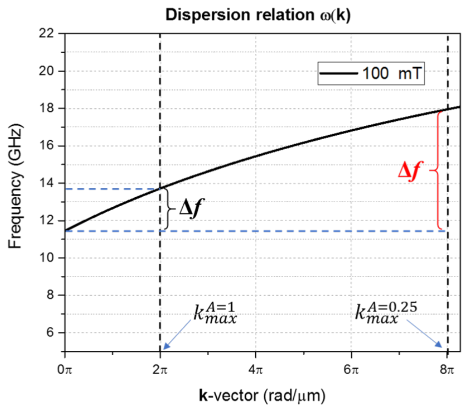

(B) Dispersion relation $f(\boldsymbol{k})$

FIGURE 4.10: Influence of the antenna width A. (A) Signal measured with $W = 5\mu m$, $d = 10\ nm$, $P = 1\ \mu$ at $H_0 =\ mT$ for two different A. The amplitude of the signal decrease with A. (B) Dispersion relation of the MSSW mode at $H_0 = 100\ mT$ and $M_s = 1250\ emu/cm^3$. The maximum k_{max} increase with the scaling down of the antenna, increasing the frequency band of the signal.

A decay by a factor 40 in the signal amplitude is observed. The first cause is the increase of the resistance decreasing, therefore, the current in the smallest antenna. The second reason comes from the causative coupling between the antenna and the substrate when the current density injected in the antenna for the emission increase with the scaling down, as explained at the end of section 4.2. The power lost in the substrate decrease the amplitude of the signal, making it harder to detect. A way to solve this issue could be the used of an insulating substrate in future experiments, like sapphire or high resistive Silicon

4.3.4 Waveguide width W

Now the scale down of the waveguide width W is studied for a device with $d = 10\ nm$, $P = 1\ \mu m$, $A = 250\ nm$ at $H_0 = 100\ mT$. Fig.4.11 shows the signal for two different waveguides width of 5 μm and 20 μm. Since the external field is the same, the FMR and the dispersion relation are the same resulting in the same frequency band as well as the same phase rotation since the propagation distance $\boldsymbol{r}$ is also the same. However, the amplitude of the signal decreases while scaling the width because the detected current intensity depends on the magnetic volumes (i.e., the total magnetic moment that generates an electrical current) that decreases with the width.

To scaling down furthermore the width without decreasing the signal amplitude, the devices implement parallel waveguides to keep the magnetic volume equal to the magnetic volume of a waveguide of $W = 5\ \mu m$. Fig.4.11 shows the signal of these devices with one waveguide $W = 5\ \mu m$, two waveguides of 2.5 μm and twenty waveguides of 250 nm.

These curves show a shift of their band to lower frequency when W decreases. The reason comes from the shape anisotropy created by the finite waveguide width that became dominant below 5 μm. The demagnetization field (see section) reduces the internal field inside the waveguide when the width decrease and therefore, shifts

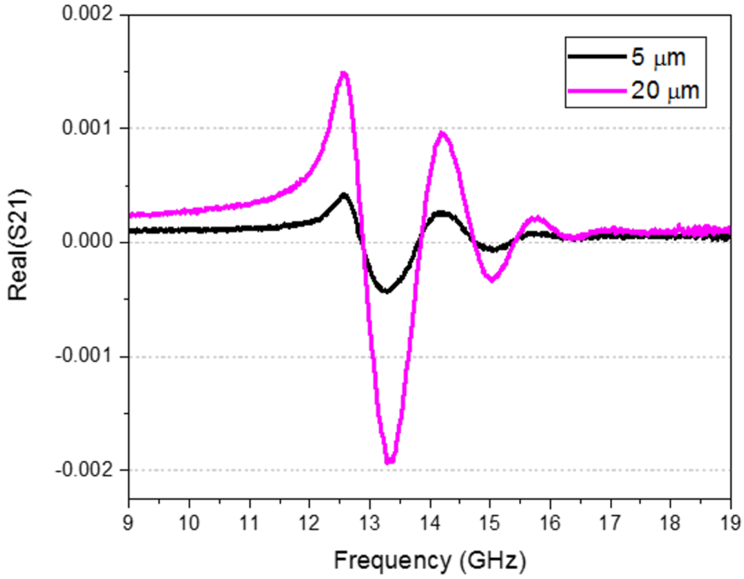

FIGURE 4.11: Influence of the waveguide with W with $d = 10\ nm$, $P = 1\ \mu m$, $A = 250\ nm$ at $H_0 = 100\ mT$ for $W = 20\ \mu m$ and $W = 5\ \mu m$.

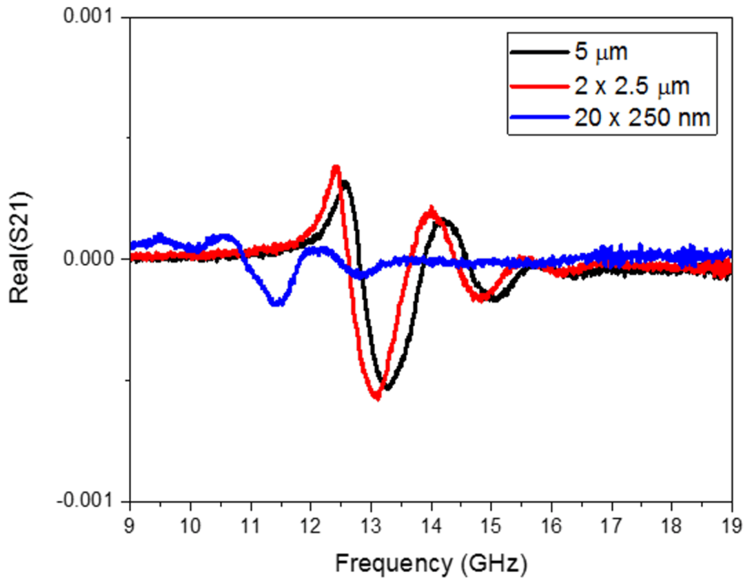

FIGURE 4.12: Influence of the waveguide with W with $d = 10\ nm$, $P = 1\ \mu m$, $A = 250\ nm$ at $H_0 = 100\ mT$. The band shift is caused by the decreased of the internal field due to the shape anisotropy.

the frequency band to the left. The decrease in the 250 nm waveguides suggest that the decay length in ultra scaled structures is different.

4.4 Free layer thickness d

Finally, the influence of the free layer thickness d is studied. The equation (4.12) shows that the evolution of the dispersion relation changes with the thickness of the film. When d decreases, the slope of the curve decreases, and therefore, for the same range of $\boldsymbol{k}$-vector, the frequency band shrinks with d but starting technically, at the same FMR as illustrated in the Fig.4.13.

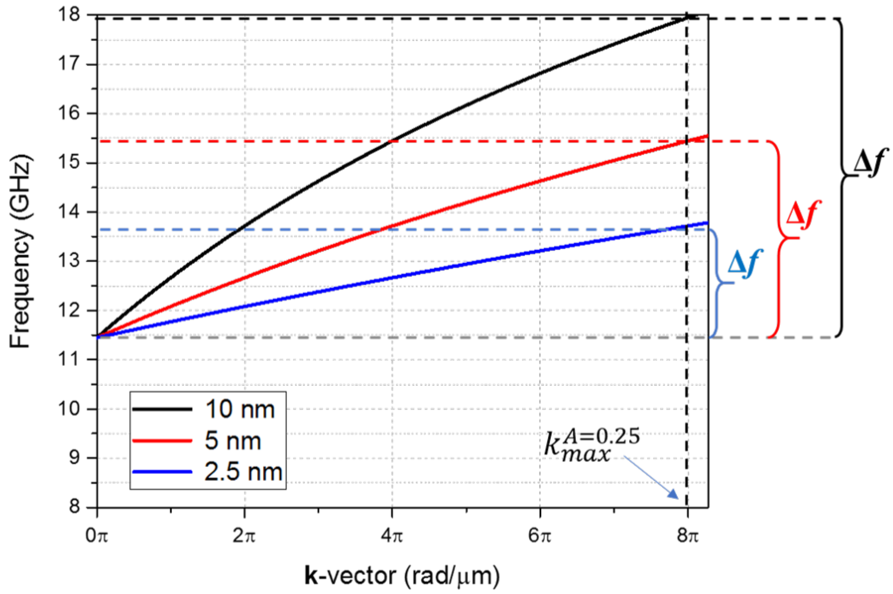

FIGURE 4.13: Dispersion relation of the MSSW mode for the three free layer thickness (with $H_0 = 100\ mT$). The FMR remains the same for the three thickness, and the frequency band is broader when d increases (the bands are shown for a $k_{max} = 2\pi/0.25\ (rad/\mu m)$).

Fig.4.14a shows the signal at $H_0 = 35\ mT$ for the three different free layer thicknesses with the corresponding dispersion relation computed from (4.12) with $W = 20\ \mu m$, $A = 250\ nm$ and $P = 2\mu m$. As expected, the signal band shrinks when d decreases. However, a shift of the FMR is observed compared to the expected value (indicated with dashed line on the curve). The thicker layer has a shifted band to higher frequency and the thinner layer shifts in the opposite direction. Fig.4.14b and Fig.4.14c show that this shift increases with the external field.

This effect can have different origin; one reason could come from an incorrect calibration of the external field during the measurement, meaning that the real field could be different and explain a shift of the band from the expectation. Nevertheless, in this case, the variation should be the same for every thickness and therefore, does not explain the relative shift of the curve with d and why it increases with the external field. In the rest of this section, different hypothesis are presented to explain this effect. Notice that they are assumptions for the time being and that further investigations have to be performed to explain these phenomena.

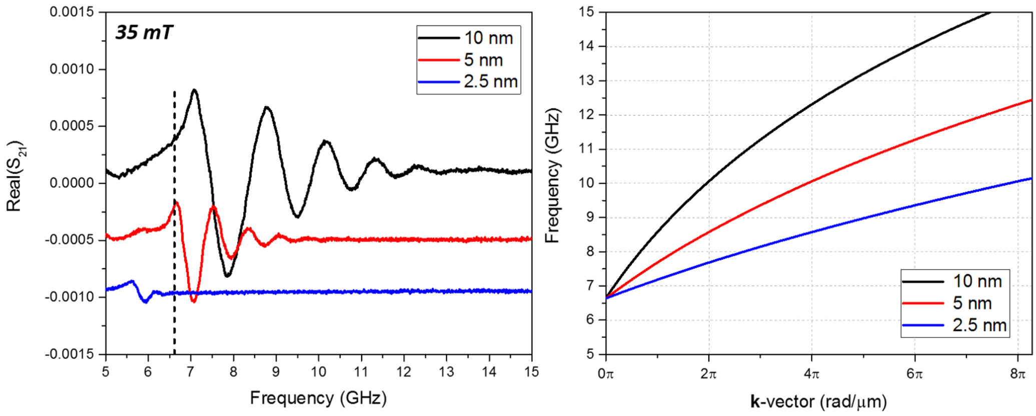

(A) $H_0 = 35\ mT$

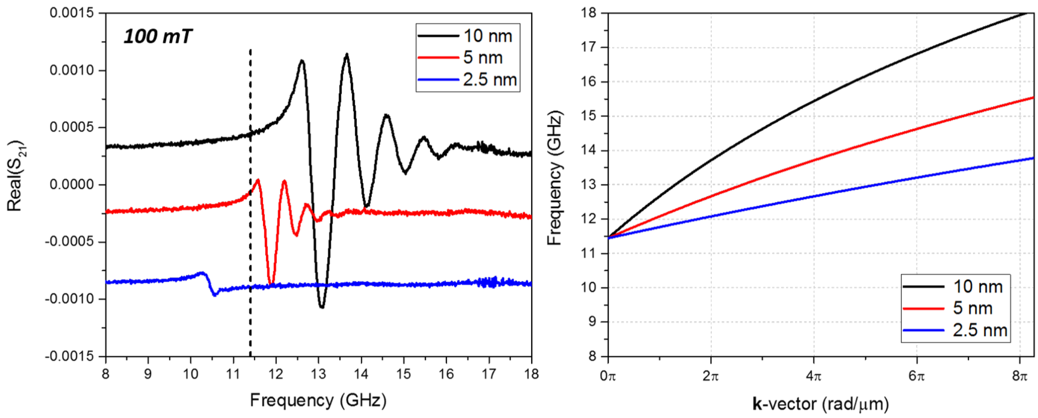

(B) $H_0 = 100\ mT$

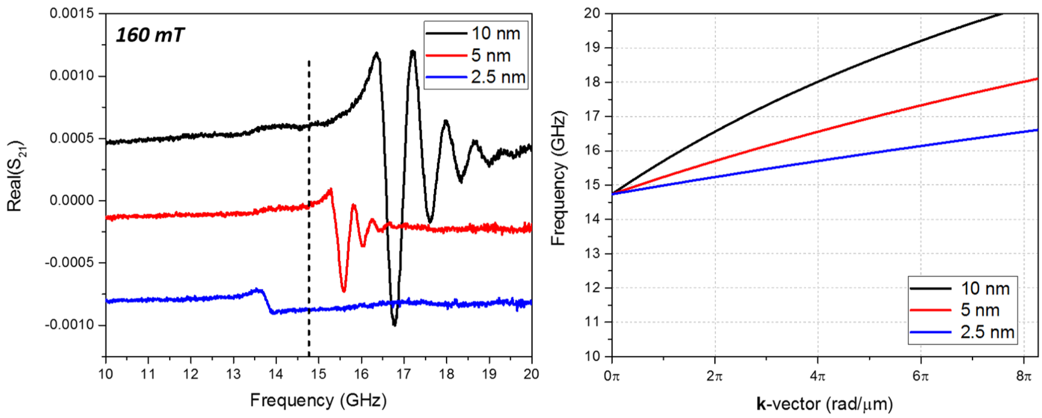

(C) $H_0 = 160\ mT$

FIGURE 4.14: Evolution of the signal with the free layers thickness d for three different external fields. The device used for the measurement has the following parameters: $W = 20\ \mu\ m$, $A = 250\ nm$ and $P = 2\ \mu m$. At low field, the experimental FMR start close to the analytical FMR, when the field increases a shift on the right is observed for the thicker layer ($d = 10\ nm$) and of shift on the right for the thinner layer ($d = 2.5\ nm$). These results are unexpected for spin wave propagation, indicating a possible influence of the perpendicular layers above the stack.

Effect of the demagnetization field H_{demag}

The dispersion relation (4.12) does not take into account the decrease of the internal field due to the demagnetization field. Micromagnetic simulations have been done to compute H_{demag}, taking into account the width of the waveguide and the thickness of the free layer but without considering the perpendicular layers above. From these simulations, the internal field H_0 is equal to:

$$H_0 = H_{ext} - H_{demag}, \tag{4.14}$$

where H_{ext} is the external field applied. Fig.4.15 shows the internal field as a function of the profile section of a 5 μm waveguide, for an external field of $H_{ext} = 35\ mT$ and $H_{ext} = 160\ mT$. These curves show that the demagnetization field has a small influence on the internal field. H_{demag} decreases the field of maximum 2 mT for the thinnest layer and, does not change significantly with H_{ext}. Moreover, H_{demag} is higher when the free layer is thicker (i.e., lower internal field), meaning that the thicker layer should have a band shift on the left compared to the thinner layer, yet the experimental data show the opposite trend. Therefore, these simulations show that the effect of the demagnetization field is not a dominant effect on the band shift and that other phenomena are responsible for the change of the FMR and the dispersion relation.

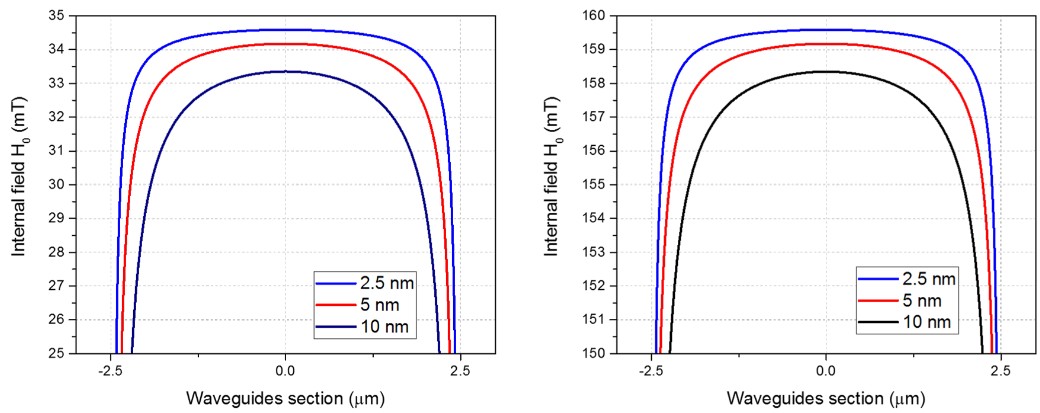

(A) $H_{ext} = 35\ mT$ (B) $H_{ext} = 160\ mT$

FIGURE 4.15: Micromagnetic simulation of the demagnetization field for a thin film of CoFeB with three different thickness and a waveguide width of 5 μm. The simulation doesn't take into account the perpendicular layers above.

Effect of the stray field created by perpendicular layers

At zero field, the perpendicular layers (PLs) are pinned out-of-plane, and the stray field generated by these layers in the free layer is perpendicular to the waveguide; therefore, the stray field does not affect the internal field oriented in-plane. When the external field increases, the PLs start to tilt in-plane. The magnetic component of the magnetic moment in these layers generates a stray field inside the free layer in the opposite direction of the magnetization. Therefore, the internal field decreases when the external field increases.

As shown in Fig.4.16, it is possible to estimate the tilted angle of the PLs magnetization as a function of the external field from the VSM measurement:

$$\frac{M_{s(PLs)} - \Delta M(H_0)}{M_{s(PLs)}} = cos(\theta), \tag{4.15}$$

where $M_{s(PLs)}$ is the magnetic saturation of the PLs and ΔM is the magnetic moment measured at a given external field minus the magnetic saturation of the free layer $M_{s(FL)}$.

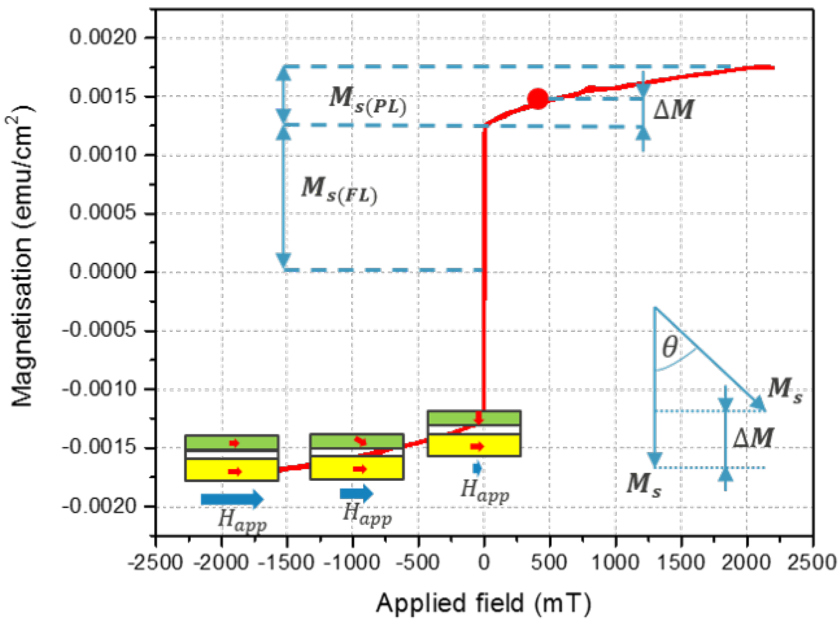

FIGURE 4.16: VSM measurement with the external field in-plane. From the magnetic moment measured at a given field, it is possible to estimate the angle of the magnetization inside the perpendicular layers.

The estimated angles for the corresponding field are the following:

- $\theta_{35mT} \approx 20°$
- $\theta_{100mT} \approx 30°$
- $\theta_{160mT} \approx 35°$

It means that for these fields, the PLs are already significantly tilted and therefore the generated stray field may reduce the internal field of the free layer. It is consistent with the fact that the shift is stronger when the external field increases since the tilted angle (and thus the stray field) increases with the external field. Furthermore, since the stray field decays with the distance, it is coherent that the effect is higher for the thinnest layer and it explains why the band of the 2.5 nm layer is more shifted on the left than the 10 nm. Nevertheless, it does not justify the band shift on the right (that correspond to an increase of the internal field).

Mixed mode between MSSW and FVMSW

As explained in chapter 3, due to the interfacial effect between the MgO and the $CoFeB$ layer, the magnetization of $CoFeB$ is pinned out-of-plane (PMA). Nevertheless, since interface anisotropy is limited to very short distance ($\approx 1\ nm$), the free layer has been considered fully magnetized in-plane. The deviation of the expected behavior could originate from this assumption.

For a thick layer (far above 10 nm), the PMA does not affect the wave, and the propagation mode is the MSSW mode considered until here. For a thin layer (below 1 nm), the magnetization is fully out-of-plane, in this case, the propagating mode is the forward volume magnetostatic mode (FVMSW); for this mode, the FMR is not $FMR_{MSSW} = \gamma\mu_0\sqrt{H_0\left(H_0 + M_s\right)}$, but $FMR_{FVMSW} = \gamma\mu_0 H_0$ (see section1.4.1).

Therefore, the mode of propagation here could be a mix of these two modes. It is consistent with the fact that the FMR in the FVMSW mode is lower. The propagation in the thinnest layer is closer to the FVMSW propagation and therefore have a smaller FMR, closer to the FMR_{FVMSW}. For the thicker layers, the propagation starts at a higher FMR closer to the FMR_{MSSW}. The evolution of the FMR with the internal field H_0 in a mixed mode between MSSW and FVMSW can be expressed with the empirical expression:

$$FMR = \gamma\mu_0\sqrt{H_0\left(H_0 + M_s\left(1 - e^{-\sqrt{\frac{d}{\lambda}}}\right)\right)}, \tag{4.16}$$

where d is the thickness of the free layer and λ an empirical parameter with length units. When d is high, the expression return to the FMR_{MSSW} expression, and when d is small, the expression tends to FMR_{FVMSW}, as shown in Fig.4.17. The figure also explains why the relative shift of the FMR between the different thickness increases with H_0.

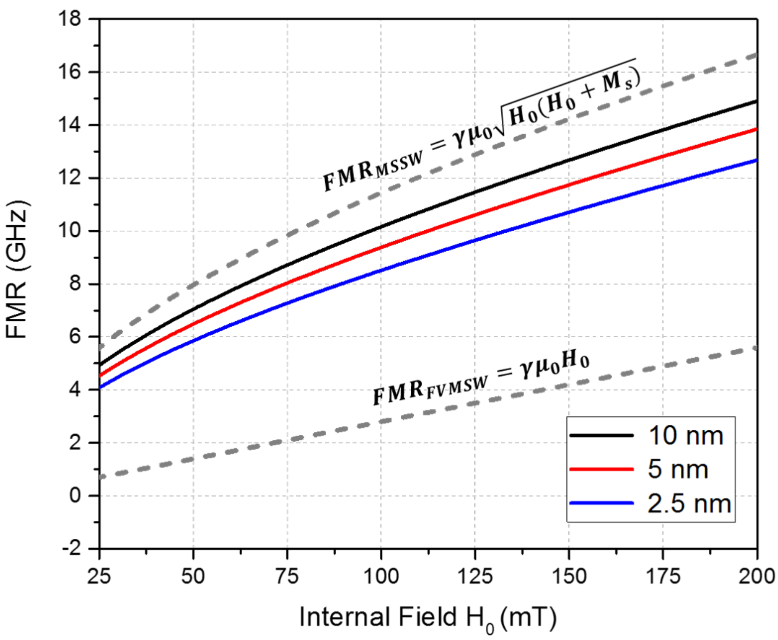

FIGURE 4.17: Evolution of the FMR with the internal field for a mixed mode between the MSSW and FVMSW. The curve are computed from the equation (4.16) with $\lambda = 4.5\ nm$. In dash line, the evolution of the FMR for the MSSW and the FVMSW.

From this expression (with λ set to 4.5 nm), the FMR shift is around 1 GHz between the three curves at $H_0 = 160\ mT$ and 0.5 GHz at 35 mT; it is more or less the case in the experimental curves even though the shift between the 5 nm and 2.5 nm is higher than this value. It is likely that the FMR in the thinnest layers is even more shifted due to a decrease of the internal field as well. Indeed, in the assumption that for a thin layer the magnetization is tilted partially out-of-plane, the internal field H_0 is not mostly due to the external field but to the field originating from the pinning of the magnetization at the interface due to the PMA.

Nevertheless, this effect, as well as the effect of the stray field presented before, does not explain the right shift of the FMR in the measurements. It is possible that due to a wrong calibration of the field, H_0 is, in reality, higher and that one, or even both, of the two last effect presented, are responsible for the left shift of the curves. Once again, they are only assumptions and detailed measurements, as well as micromagnetic simulations of the full stack, has to be done to understand these effects fully.

4.5 Conclusion

In this chapter, the measurement of the two antenna devices has been detailed. The typical behavior of spin wave propagation for a surface mode (MSSW) has been observed. The data were presented for the 10 nm free layer, but the devices, with different thicknesses, show the same evolution with the parameters. The signal observed is lower in the thinner films due to a decrease in the magnetic volume. Nevertheless, spin wave signal is still detected in the thinnest film of 2.5 nm even though at higher fields the phase rotations disappear and only the FMR peak is detected as shown in Fig.4.18.

The comparison of the data for different free layer thickness shows a shift of the frequency band as a function of the field and the thickness. Since these effects have not been observed before, this indicated that the perpendicular layer has most probably an influence on the propagating properties of the wave, due to another kind of propagating mode in this structure or due to a change of the internal field inside the free layer caused by the other layers.

Further investigation has to be done to understand the origin of this effect fully. The complex dynamic of this system requires micromagnetic simulation to identify the different mechanisms in play during the propagation. Simulation, as well as more precise measurements with a lower noise level and a higher number of field points, are also required to detect potential other modes, in the reference layer, or even in the SAF similar to what has already been reported [39].

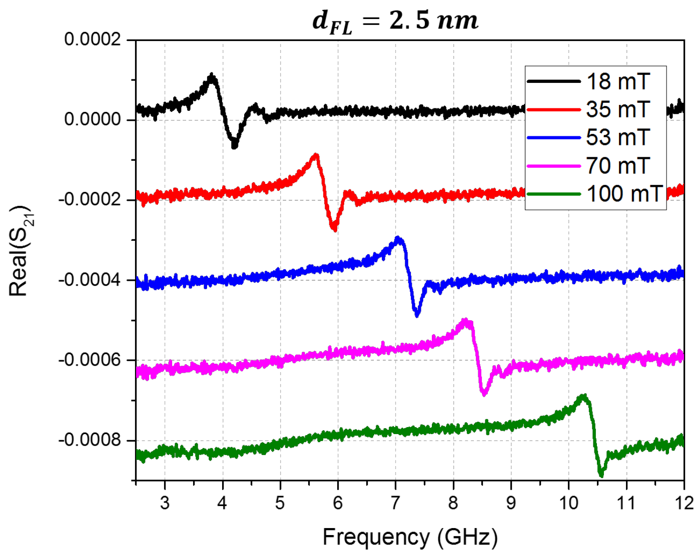

FIGURE 4.18: Evolution of the propagation with the field for devices with a free layer thickness $d = 2.5\ nm$ with $W = 5\ \mu$, $A = 250\ nm$ and $P = 1\ \mu m$. At higher fields, the phases rotation are not detected

Conclusion

In this thesis, the development of two spin wave devices based on an orthogonal MTJ stack has been presented. One for the study of spin waves propagation inside the magnetic stack using antenna transducers and one to characterize the emission of spin wave by STNO.

The material characterization of the MTJ stack shows that the perpendicular layers used to polarized a spin current are made of a hard ferromagnet and that the free layer has the properties of a soft magnet; therefore the magnetic stack is suitable for spin waves emission by STT. The antenna devices have been completely fabricated, and the STNO devices are under fabrication after full development of the process. SEM inspection of the antenna devices shows a proper fabrication with a feature size slightly larger compared to the nominally defined in the design and that a too far recession during the planarization has generated a non-perfectly flat antenna.

Nevertheless, the electrical characterization shows that less than 5% of the devices have broken antennas (open circuit) or poor insulation with the waveguide (short circuit between the two antennas). The RF measurements show a typical signature of spin wave propagation in the free layer for the MSSW mode. This is observed also in the thinnest free layer (2.5 nm) although the phase rotations are vanishing after a certain external applied field. This phenomenon still needs understanding.

The spin wave signals measured present a shift in their ferromagnetic frequency for a given applied field, compared to the expected value. The deviation could originate from a wrong calibration of the magnetic field. However, it does not explain the relative shift of the frequency bands with the free layer thickness, at the same applied field. It has been shown that the demagnetization field cannot be responsible for these effects. Therefore, it can be concluded that these shifts originate from the influence of the perpendicular layers on the spin wave propagation inside the free layers. Various possible explanations have been proposed, yet micromagnetic simulations need to be performed to understand the complex dynamic inside this multi-layers stack.

In this study, no other mode of propagation has been detected. Nevertheless, the propagation of additional modes with lower amplitude was challenging to detect in the brand new magneto-setup in IMEC. More accurate measurements with a lower noise level and a higher number a field points are required to potentially identify them.

This work was only the starting point of the development for this kind of devices, and this technology still requires multiple investigations to be fully understood. When the dynamic of the propagation inside the stack will be sufficiently understood, the electrical measurement of STNO devices will allow the study of the efficiency of this transducers. Note that the current flowing through the pillar will generate Oersted field in the waveguide and will influence also the propagation properties. Finally, the capability of the transducers to detect a spin wave signal has to been demonstrated. Technically the spin wave can be identified by TMR in the pillar, but its efficiency and sensitivity, considering the small angle precession, still need to be proved. This study and its completeness will lead to identify a possible route for spin wave logic circuit where STT and TMR are used as physical effects for transduction.

Bibliography

[1] Mohammed Zidan, John William Strachan, and Wei Lu. "The future of electronics based on memristive systems". In: *Nature Electronics* 1 (Jan. 2018), pp. 22–29. DOI: 10.1038/s41928-017-0006-8.

[2] Hugh D. Young. "University Physics". In: ed. by Addison-Wesley 8th Ed. 1992.

[3] W. Heisenberg. "Zur Theorie des Ferromagnetismus". In: *Zeitschrift für Physik* 49.9 (Sept. 1928), pp. 619–636. ISSN: 0044-3328. DOI: 10.1007/BF01328601. URL: https://doi.org/10.1007/BF01328601.

[4] Alexy D. Karenowska et al. "Magnon Spintronics". In: *Handbook of Spintronics*. Ed. by Yongbing Xu, David D. Awschalom, and Junsaku Nitta. Dordrecht: Springer Netherlands, 2014, pp. 1–38. ISBN: 978-94-007-7604-3. DOI: 10.1007/978-94-007-7604-3_53-1. URL: https://doi.org/10.1007/978-94-007-7604-3_53-1.

[5] Thomas A. Gilbert. "A phenomenological theory of damping in ferromagnetic materials". In: *IEEE Transactions on Magnetics* 40 (2004), pp. 3443–3449.

[6] Alexander Makarov. "Modeling of Emerging Resistive Switching Based Memory Cells". PhD thesis. Mar. 2014. DOI: 10.13140/RG.2.2.11456.74242.

[7] P. Gambardella. "Introduction to spin torques and spin-orbit torques in metal layers". In: ed. by ETH Zurich. 2015. URL: https://www.ethz.ch/content/dam/ethz/special-interest/matl/intermag-dam/Publications/Talks/PG_Tutorial_Munich_STT_SOT.pdf.

[8] J. C. Slonczewski. "Excitation of spin waves by an electric current". In: *Journal of Magnetism and Magnetic Materials* 195 (1999), pp. L261–L268. DOI: 10.1016/S0304-8853(99)00043-8.

[9] Florin Ciubotaru. "Spin-wave excitation by nano-sized antennas". PhD thesis. Citeseer, 2012.

[10] F. Bloch. "Zur Theorie des Ferromagnetismus". In: *Zeitschrift für Physik* 61.3 (Mar. 1930), pp. 206–219. ISSN: 0044-3328. DOI: 10.1007/BF01339661. URL: https://doi.org/10.1007/BF01339661.

[11] T. Holstein and H. Primakoff. "Field Dependence of the Intrinsic Domain Magnetization of a Ferromagnet". In: *Phys. Rev.* 58 (12 Dec. 1940), pp. 1098–1113. DOI: 10.1103/PhysRev.58.1098. URL: https://link.aps.org/doi/10.1103/PhysRev.58.1098.

[12] Freeman J. Dyson. "General Theory of Spin-Wave Interactions". In: *Phys. Rev.* 102 (5 June 1956), pp. 1217–1230. DOI: 10.1103/PhysRev.102.1217. URL: https://link.aps.org/doi/10.1103/PhysRev.102.1217.

[13] Conyers Herring and Charles Kittel. "On the Theory of Spin Waves in Ferromagnetic Media". In: *Phys. Rev.* 81 (5 Mar. 1951), pp. 869–880. DOI: 10.1103/PhysRev.81.869. URL: https://link.aps.org/doi/10.1103/PhysRev.81.869.

[14] B. A. Kalinikos and A. N. Slavin. "Theory of dipole-exchange spin wave spectrum for ferromagnetic films with mixed exchange boundary conditions". In: *Journal of Physics C Solid State Physics* 19 (Dec. 1986), pp. 7013–7033. DOI: 10.1088/0022-3719/19/35/014.

[15] Sergej O. Demokritov. "Magnons". In: *Topology in Magnetism*. Ed. by Jiadong Zang, Vincent Cros, and Axel Hoffmann. Cham: Springer International Publishing, 2018, pp. 299–334. ISBN: 978-3-319-97334-0. DOI: 10.1007/978-3-319-97334-0_10. URL: https://doi.org/10.1007/978-3-319-97334-0_10.

[16] Daniel D. Stancil and Anil Prabhakar. "Propagation Characteristics and Excitation of Dipolar Spin Waves". In: *Spin Waves: Theory and Applications*. Boston, MA: Springer US, 2009, pp. 169–202. ISBN: 978-0-387-77865-5. DOI: 10.1007/978-0-387-77865-5_6. URL: https://doi.org/10.1007/978-0-387-77865-5_6.

[17] AV Chumak et al. "Magnon spintronics". In: *Nature Physics* 11.6 (2015), p. 453.

[18] M. Mitchell Waldrop. "The chips are down for Moore's law". In: *Nature News* 530 (Feb. 2016), pp. 144–147. DOI: doi:10.1038/530144a.

[19] IEEE. *International Roadmap for Devices and Systems (IRDS^{TM})*. https://irds.ieee.org/. 2016.

[20] Wolfgang ARDEN. "More-than-Moore White Paper". In: *ITRS (Int. Tech. Roadmap for Semiconductors)* (2011). URL: https://ci.nii.ac.jp/naid/10031112063/en/.

[21] R Compano, L Molenkamp, and DJ Paul. "Roadmap for nanoelectronics". In: ().

[22] Luca Amarú, Pierre-Emmanuel Gaillardon, and Giovanni De Micheli. "Majority-Inverter Graph: A Novel Data-Structure and Algorithms for Efficient Logic Optimization". In: (June 2014).

[23] Kavita Khare and Krishna Dayal Shukla. "Design A 1Bit Low Power Full Adder Using Cadence Tool". In: *AIP Conference Proceedings* 1324.1 (2010), pp. 373–376. DOI: 10.1063/1.3526237. eprint: https://aip.scitation.org/doi/pdf/10.1063/1.3526237. URL: ttps://aip.scitation.org/doi/abs/10.1063/1.3526237.

[24] Odysseas Zografos et al. "Spin-Based Majority Computation". In: *Beyond-CMOS Technologies for Next Generation Computer Design*. Ed. by Rasit O. Topaloglu and H.-S. Philip Wong. Cham: Springer International Publishing, 2019, pp. 231–262. ISBN: 978-3-319-90385-9. DOI: 10.1007/978-3-319-90385-9_7. URL: https://doi.org/10.1007/978-3-319-90385-9_7.

[25] Á. Papp et al. "Spin-wave-based computing devices". In: *14th IEEE International Conference on Nanotechnology*. Aug. 2014, pp. 96–99. DOI: 10.1109/NANO.2014.6968127.

[26] S. Breitkreutz-von Gamm et al. "Design of On-Chip Readout Circuitry for Spin-Wave Devices". In: *IEEE Magnetics Letters* 8 (2017), pp. 1–4. ISSN: 1949-307X. DOI: 10.1109/LMAG.2016.2618779.

[27] T. Fischer et al. "Experimental prototype of a spin-wave majority gate". In: *Applied Physics Letters* 110.15 (2017), p. 152401. DOI: 10.1063/1.4979840. eprint: https://doi.org/10.1063/1.4979840. URL: https://doi.org/10.1063/1.4979840.

[28] Sourav Dutta et al. "Proposal for nanoscale cascaded plasmonic majority gates for non-Boolean computation". In: *Scientific Reports*. 2017.

[29] F. Ciubotaru et al. "First experimental demonstration of a scalable linear majority gate based on spin waves". In: *2018 IEEE International Electron Devices Meeting (IEDM)*. Dec. 2018, pp. 36.1.1–36.1.4. DOI: 10.1109/IEDM.2018.8614488.

[30] A A Serga, A V Chumak, and B Hillebrands. "YIG magnonics". In: *Journal of Physics D: Applied Physics* 43.26 (June 2010), p. 264002. DOI: 10.1088/0022-3727/43/26/264002. URL: https://doi.org/10.1088%2F0022-3727%2F43%2F26%2F264002.

[31] A. Slavin and V. Tiberkevich. "Nonlinear Auto-Oscillator Theory of Microwave Generation by Spin-Polarized Current". In: *IEEE Transactions on Magnetics* 45.4 (Apr. 2009), pp. 1875–1918. ISSN: 0018-9464. DOI: 10.1109/TMAG.2008.2009935.

[32] Grégoire de Loubens and Matthieu Bailleul. "Microwave Nanomagnetism: Spin Torque Oscillators and Magnonics: Applications and Perspectives". In: Mar. 2017, pp. 269–296. ISBN: 9783527339853. DOI: 10.1002/9783527698509.ch12.

[33] Vladislav E Demidov, Sergei Urazhdin, and So Demokritov. "Direct observation and mapping of spin waves emitted by Spin-torque nano-oscillators". In: *Nature materials* 9 (Oct. 2010), pp. 984–8. DOI: 10.1038/nmat2882.

[34] S Urazhdin et al. "Nanomagnonic devices based on the spin-transfer torque". In: *Nature nanotechnology* 9 (May 2014). DOI: 10.1038/nnano.2014.88.

[35] Mohsin Rafique. "Study of the Magnetoelectric Properties of Multiferroic Thin Films and Composites for Device Applications". PhD thesis. Mar. 2015.

[36] Min Zhao et al. "Technology of alignment mark in electron beam lithography". In: vol. 9285. Aug. 2014, p. 92850C. DOI: 10.1117/12.2068112.

[37] K Kurokawa. "Power Waves and the Scattering Matrix". In: *Microwave Theory and Techniques, IEEE Transactions on* 13 (Apr. 1965), pp. 194–202. DOI: 10.1109/TMTT.1965.1125964.

[38] F. Ciubotaru et al. "All electrical propagating spin wave spectroscopy with broadband wavevector capability". In: *Applied Physics Letters* 109.1 (2016), p. 012403. DOI: 10.1063/1.4955030. eprint: https://doi.org/10.1063/1.4955030. URL: https://doi.org/10.1063/1.4955030.

[39] W Zhou. "Spin Waves Excitations of Co/Pt Multilayers". In: *Journal of Nanomaterials* 2012 (Oct. 2012). DOI: 10.1155/2012/496519.

UNIVERSITÉ CATHOLIQUE DE LOUVAIN
École polytechnique de Louvain
Rue Archimède, 1 bte L6.11.01, 1348 Louvain-la-Neuve, Belgique | **www.uclouvain.be/epl**